

PAPER • OPEN ACCESS

# Large-scale vortex formation in three-dimensional rotating Rayleigh-Bénard convection

To cite this article: Hirofumi Sasaki *et al* 2024 *Fluid Dyn. Res.* **56** 035504

View the [article online](#) for updates and enhancements.

You may also like

- [Large-scale Vortices in Rapidly Rotating Rayleigh-Bénard Convection at Small Prandtl number](#)  
Tao Cai
- [North alignment of multi-rotating systems using a known fixed point](#)  
Meysam Yadegar and Farzaneh Karami
- [Velocimetry in rapidly rotating convection: Spatial correlations, flow structures and length scales](#)  
Matteo Madonia, Andrés J. Aguirre Guzmán, Herman J. H. Clercx *et al.*

# Large-scale vortex formation in three-dimensional rotating Rayleigh-Bénard convection

Hirofumi Sasaki, Shin-ichi Takehiro\*  and Michio Yamada

Research Institute for Mathematical Sciences, Kyoto University, Sakyo-ku, Kyoto 606-8502, Japan

E-mail: [takepiro@gfd-dennou.org](mailto:takepiro@gfd-dennou.org), [hirofumi@kurims.kyoto-u.ac.jp](mailto:hirofumi@kurims.kyoto-u.ac.jp) and [yamada@kurims.kyoto-u.ac.jp](mailto:yamada@kurims.kyoto-u.ac.jp)

Received 18 January 2024; revised 11 May 2024

Accepted for publication 2 June 2024

Published 14 June 2024

Communicated by Professor Genta Kawahara



CrossMark

## Abstract

Numerical experiments are performed on three-dimensional thermal convection between parallel plates in a rotating system with a larger horizontal region than in previous studies. It is confirmed that a large-scale vortex (LSV) with positive vorticity (cyclonic) is formed over a significant part of the region and its horizontal size increases if the horizontal region is extended. The correlation analysis in the vertical direction shows that the small-scale motion has a typical structure of the baroclinic vortex of thermal convection in the rotating system, whereas the large-scale motion is a barotropic vortex that is not associated with thermal convection. A horizontal spectral analysis of the individual terms in the kinetic energy equation reveals that the nonlinear effect of the small-scale vortex motion caused by the buoyancy force induces a large-scale toroidal component, and that the LSV is maintained by the balance between the nonlinear effect and the viscous dissipation of the large-scale motion. The results of this analysis indicate the importance of kinetic energy damping mechanism for the appearance of LSVs. When weak damping operates at larger scales, it is expected that the maximum extent of the vortex appears even if the horizontal

\* Author to whom any correspondence should be addressed.



Original Content from this work may be used under the terms of the [Creative Commons Attribution 4.0 licence](https://creativecommons.org/licenses/by/4.0/). Any further distribution of this work must maintain attribution to the author(s) and the title of the work, journal citation and DOI.

region is extended further. On the other hand, the emergence of LSVs will be prevented when strong enough damping is effective at larger scales.

Keywords: rotating fluid, thermal convection, coherent vortex

## 1. Introduction

The problem of thermal convection in rotating systems has been studied for a long time in connection with fluid phenomena on and within the surfaces of stars and planets, including meteorological and oceanic phenomena. The problem of Rayleigh–Bénard convection between parallel plates in a rotating system is one of the most fundamental model setups. The classical linear stability theory shows that the horizontal scale of the thermal convective motion becomes smaller, and the structure elongated in the direction of the rotation axis becomes dominant as the angular velocity of the rotating system increases (e.g. Chandrasekhar 1961). On the other hand, numerical calculations of three-dimensional finite amplitude thermal convection showed that horizontally large-scale vortices (LSVs) emerge in rapidly rotating cases (Julien *et al* 2012, Favier *et al* 2014, Guervilly *et al* 2014). This phenomenon had already been found in earlier studies on compressible convection (Chan 2007, Käpylä *et al* 2011). Since the emergence of the coherent large-scale structure excited by small-scale thermal convection seems to be related to the formation of large-scale vortices in the planetary atmospheres such as Jupiter’s Great Red Spot (e.g. Chan and Mayr 2013), the phenomenon has attracted the interest of researchers, and has continued to be studied intensively.

For LSVs to emerge, the Rossby number must be small so that the effect of rotation is sufficient to influence convective motion. LSVs do not form when the Rayleigh number is too large (Favier *et al* 2014). Spectral analysis, which separates the kinetic energy from horizontal fluid motion and that from vertical fluid motion, suggested that the contribution of non-local energy transport due to non-linear effects of small-scale horizontal motion is significant, rather than an inverse cascade observed in two-dimensional turbulence (Favier *et al* 2014, Guervilly *et al* 2014). Favier *et al* (2019) performed numerical experiments taking a strong large-scale vortex as initial conditions, and showed that the formation of LSVs is subcritical and also confirmed the importance of energy transport by the non-local large-scale field. de Wit *et al* (2022) performed numerical experiments varying the Rayleigh number and found that there exists hysteresis and discontinuity in the transition to the LSV emergent state.

A reduced system derived by taking the limit of very rapid rotation (so called non-hydrostatic quasi-geostrophic equations; NH-QGEs) has also been proposed (Julien *et al* 1998, Julien and Knobloch 2007) and the behaviors of the solutions of the system are discussed based on numerical experiments (e.g. Sprague *et al* 2006, Julien *et al* 2012, 2018, Rubio *et al* 2014, Maffei *et al* 2021). Julien *et al* (2012) performed numerical experiments varying the Rayleigh number and the Prandtl number. They carried out detailed statistical analysis to characterize the flow in each regime, and LSVs are observed in the geostrophic turbulence regime of the experiments. Rubio *et al* (2014) has performed numerical experiments over a larger computational domain in the horizontal direction, observed the emergence of large-scale vortices, and argued that emergence of LSVs is due to positive feedback between large-scale barotropic vortices and small scale convective eddies. Julien *et al* (2018) performed numerical experiments for the case where the computational domain is a horizontally elongated rectangular area, and found a solution where the square regions of positive and negative vorticity are aligned horizontally. Maffei *et al* (2021) investigate the inverse cascade and scaling properties in the limit of vanishing Rossby number with much higher resolution.

These studies have examined the conditions for the formation of LSVs using horizontal spectral decomposition. However, the following points have not yet been clarified with regard to the appearance of LSVs. The spectral analysis carried out so far has only been focused on the energy transport due to the non-linear term from the point of view of whether or not it resembles two-dimensional turbulent behavior, while little attention has been paid to the role of the Coriolis and viscous terms. Large eddies are likely to have different properties with their sign. While the asymmetry of the amplitudes has been analyzed statistically (Favier *et al* 2014, Guervilly *et al* 2014), the horizontal scale difference has not been quantitatively investigated. In contrast, the reduced system produces positive-negative symmetric large eddies (e.g. Rubio *et al* 2014). It is also not certain whether the LSV always will extend to the entire computational domain or not. Spectral analysis of the motion of small-scale fields has been performed, but less attention has been paid to their properties in real space.

Therefore, in this study, we follow-up numerical simulations of three-dimensional Rayleigh-Bénard thermal convection between parallel horizontal plates in a rotating system, and investigate the formation and maintenance mechanism of LSVs. We conduct numerical experiments in which the horizontal range is larger than that of the numerical experiment by Guervilly *et al* (2014), and perform a detailed statistical analysis of LSVs and convective motion. Specifically, we decompose the velocity field into large and small scale components for both toroidal and poloidal velocities, and study the kinetic energy exchange between these components. In addition, we characterize the structure of fluid motion in the large and small scale fields by correlation analysis in the vertical direction. In the following, the model and numerical experiment are described in section 2. Section 3 presents the numerical results using the energy spectrum analysis and the correlation analysis. Based on these results, we present in section 4 a linear analysis that includes the effect of large-scale vorticity, and we discuss quantitatively the dependence of the small-scale convection on the sign of the large-scale vorticity. We also construct a model to interpret the parameter dependence of the toroidal energy concentrated in the large-scale vorticity, and support the proposed mechanism for the generation of LSVs in section 3. Section 5 is the summary.

## 2. Model and setup for numerical experiments

We consider Boussinesq fluid sandwiched between parallel horizontal square plates rotating at an angular velocity of  $\Omega$  as shown in figure 1. The temperature of the bottom plate is  $\Delta T$  higher than than the top plate. The non-dimensionalized equations are as follows.

$$\nabla \cdot \mathbf{u} = 0, \quad (1)$$

$$\frac{\partial \mathbf{u}}{\partial t} + \mathbf{u} \cdot \nabla \mathbf{u} + \mathbf{e}_z \times \mathbf{u} = -\nabla p + \frac{RE^2}{P} \theta \mathbf{e}_z + E \nabla^2 \mathbf{u}, \quad (2)$$

$$\frac{\partial \theta}{\partial t} + \mathbf{u} \cdot \nabla \theta - u_z = \frac{E}{P} \nabla^2 \theta. \quad (3)$$

These equations are non-dimensionalized by choosing the length scale as the width between the plates  $d$ , the time scale as  $1/2\Omega$ , and the temperature scale as  $\Delta T$ . Here,  $\mathbf{u} = (u_x, u_y, u_z)$ ,  $p$  and  $\theta$  are velocity, pressure, and temperature disturbance. The non-dimensional numbers appearing in the equations are the Rayleigh number  $R$ , Ekman number  $E$ , and Prandtl number  $P$ , which are respectively defined as follows:

$$R = \frac{\alpha g \Delta T d^3}{\kappa \nu}, \quad E = \frac{\nu}{2\Omega d^2}, \quad P = \frac{\nu}{\kappa}, \quad (4)$$

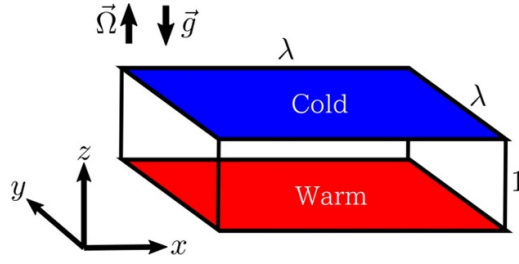


**Figure 1.** The domain for the rotating thermal convection problem.

where  $\alpha$ ,  $g$ ,  $\kappa$  and  $\nu$  are thermal expansion coefficient, gravity, thermal diffusivity and kinematic viscosity, respectively. The horizontal boundary condition is periodic. The vertical boundary conditions are fixed temperature, non-permeable, and free-slip.

$$\theta = 0, \quad \frac{\partial u_x}{\partial z} = \frac{\partial u_y}{\partial z} = u_z = 0 \quad \text{at } z = 0, 1, \quad (5)$$

From the equation of continuity (1), we can express the velocity field by mean flow  $\mathbf{U}(z, t)$ , toroidal and poloidal potentials  $\psi(x, y, z, t)$  and  $\phi(x, y, z, t)$ .

$$\mathbf{u} = \mathbf{U} + \nabla \times (\psi \mathbf{e}_z) + \nabla \times \nabla \times (\phi \mathbf{e}_z). \quad (6)$$

Substituting (6) into (1) and averaging in the horizontal direction, we have,

$$\frac{\partial U_z}{\partial z} = 0. \quad (7)$$

Then, we can find  $U_z = 0$  due to the vertical boundary condition (5), and  $\mathbf{U} = (U_x(z, t), U_y(z, t), 0)$ . Substituting (6) into (2) and averaging in the horizontal direction, we have,

$$\frac{\partial U_x}{\partial t} + \frac{\partial}{\partial z} (\overline{u_x u_z}) - U_y = E \frac{\partial^2 U_x}{\partial z^2}, \quad \frac{\partial U_y}{\partial t} + \frac{\partial}{\partial z} (\overline{u_y u_z}) + U_x = E \frac{\partial^2 U_y}{\partial z^2}. \quad (8)$$

Here,  $\overline{(\cdot)}$  means horizontal average, and the horizontally averaged pressure gradient vanishes due to periodicity.

By operating  $\mathbf{e}_z \cdot \nabla \times$ ,  $\mathbf{e}_z \cdot \nabla \times \nabla \times$  to (2), we obtain the equations for the toroidal and poloidal potentials.

$$\begin{aligned} \frac{\partial}{\partial t} \nabla_H^2 \psi + \mathbf{e}_z \cdot \nabla \times (\mathbf{u} \times \boldsymbol{\omega}) - \frac{\partial}{\partial z} \nabla_H^2 \phi &= E \nabla_H^2 \nabla^2 \psi, \\ \frac{\partial}{\partial t} \nabla_H^2 \nabla^2 \phi - \mathbf{e}_z \cdot \nabla \times \nabla \times (\mathbf{u} \times \boldsymbol{\omega}) + \frac{\partial}{\partial z} \nabla_H^2 \psi & \end{aligned} \quad (9)$$

$$= -\frac{RE^2}{P} \nabla_H^2 \theta + E \nabla_H^2 \nabla^2 \nabla^2 \phi, \quad (10)$$

where  $\nabla_H^2 \equiv \frac{\partial^2}{\partial x^2} + \frac{\partial^2}{\partial y^2}$ , and  $\boldsymbol{\omega} = (\omega_x, \omega_y, \omega_z) = \nabla \times \mathbf{u}$  is the vorticity. By expressing the temperature equation (3) with the poloidal potential, we have,

$$\frac{\partial \theta}{\partial t} + \mathbf{u} \cdot \nabla \theta + \nabla_H^2 \phi = \frac{E}{P} \nabla^2 \theta. \quad (11)$$

The vertical boundary conditions (5) become,

$$\theta = \frac{\partial\psi}{\partial z} = \phi = \frac{\partial^2\phi}{\partial z^2} \quad \text{at } z = 0, 1. \quad (12)$$

The initial condition for the numerical experiments is the state at rest with the diffusive temperature field superposed by a small pointwise temperature disturbance. The values of the non-dimensional parameters are given as  $P = 1, E = 10^{-4}, \tilde{R} \equiv RE^{4/3} = 37$  by following the experiments S1-S3 in Guervilly *et al* (2014). The horizontal extent of the domain (aspect ratio)  $\lambda$  is varied with 1, 2, 4 and 8, while Guervilly *et al* (2014) performed the cases with  $\lambda \leq 4$ .

For the numerical calculations, (8)–(12) are spatially discretised by a spectral method. The physical variables are expressed by the double Fourier series in the horizontal directions and by the Chebyshev polynomials in the vertical directions. The numbers of the grid points are  $64 \times \lambda$  and 64 in each horizontal direction and the vertical direction, respectively. The truncated horizontal wavenumber is  $\pm 64 \times \lambda/3$  to avoid aliasing errors, while Chebyshev polynomials are calculated up to 64 degrees. For numerical time integrations, the Crank-Nicolson scheme is adopted for the viscous and diffusion terms and the second order Adams-Bashforth scheme is used for other terms. A spectral transformation library ‘ISPACK’ ([www.gfd-dennou.org/library/ispack/](http://www.gfd-dennou.org/library/ispack/)) and its Fortran90 wrapper library ‘SPMODEL library’ ([www.gfd-dennou.org/library/spmodel/](http://www.gfd-dennou.org/library/spmodel/)) are used to realize numerical calculations.

### 3. Results

#### 3.1. Horizontal domain dependence

Figure 2 shows the distributions of the vertical vorticity  $\omega_z$  at the beginning and end of the calculations for different horizontal extents  $\lambda$  of the domain. Note that positive and negative  $\omega_z$  indicate cyclonic and anti-cyclonic vortices, respectively. In all cases, small-scale vortices are randomly distributed in the initial stage. In the case of  $\lambda = 1$ , the vorticity distribution is similar to the initial state at the final time. There is no difference in the characteristics of the vorticity distribution between its signs. As the aspect ratio increases with  $\lambda = 2, 4$  and 8, a large positive vorticity region (cyclonic LSV) becomes apparent, occupying about 1/4 of the domain at the final time. In the regions where positive vorticity dominates, a large-scale coherent structure is evident while small-scale positive eddies coexist in the interior. The characteristic time of development of the LSV appears roughly proportional to  $\lambda^2$ , which will be discussed in section 4.2 below.

Figure 3 shows the time evolution of the averaged kinetic energy  $\bar{K}$ , and its toroidal and poloidal components,  $\bar{K}^T$  and  $\bar{K}^P$ . Here, the averaged kinetic energy and its components are defined as follows.

$$\bar{K}(t) = \frac{1}{2\lambda^2} \int_V |\mathbf{u}|^2 dV, \quad (13)$$

$$\bar{K}^T(t) = \frac{1}{2\lambda^2} \int_V |\mathbf{u}^T|^2 dV, \quad \bar{K}^P(t) = \frac{1}{2\lambda^2} \int_V |\mathbf{u}^P|^2 dV, \quad (14)$$

$$\mathbf{u}^T = \nabla \times (\psi \mathbf{e}_z), \quad \mathbf{u}^P = \nabla \times \nabla \times (\phi \mathbf{e}_z), \quad (15)$$

$$\int_V dV = \int_0^1 dz \int_0^\lambda dy \int_0^\lambda dx = \lambda^2, \quad (16)$$

where  $V$  indicate the volume of the computational domain. Note that  $\bar{K}(t) = \bar{K}^T(t) + \bar{K}^P(t)$  since the integral of  $\mathbf{u}^T \cdot \mathbf{u}^P$  over the domain vanishes. In the case of  $\lambda = 1$ , the field reaches a steady state without significant change after the initial development settles down. On the other hand, when  $\lambda$  is greater than 2, after the initial development, the kinetic energy continues to

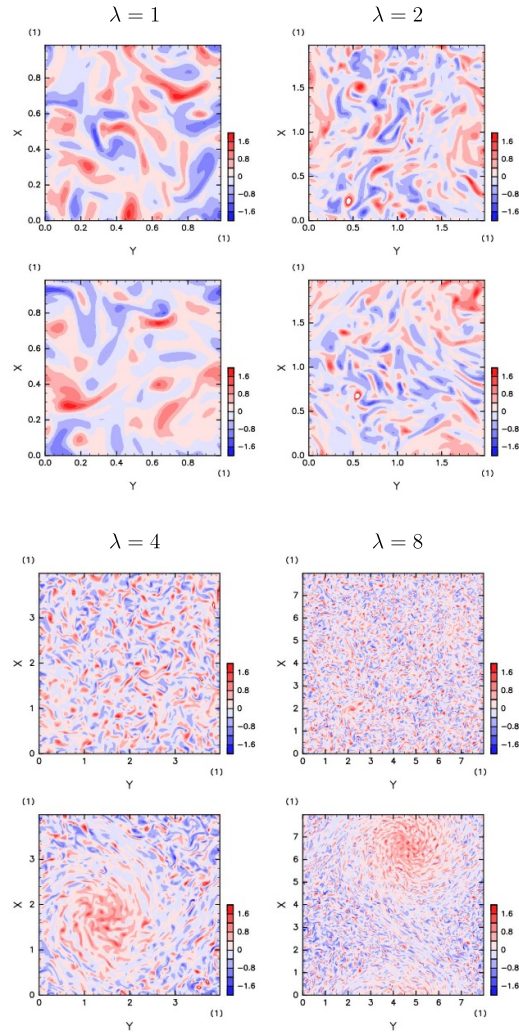


**Figure 2.** Snapshots of vertical vorticity  $\omega_z$  at  $z = 0.25$  in the transient (upper panels,  $t = 1000$ ) and final stages (lower panels). Note that positive and negative  $\omega_z$  indicate cyclonic and anti-cyclonic vortices, respectively. Times of the final stages are  $t = 30000$ ,  $30000$ ,  $50000$ , and  $52000$ , respectively.  $P = 1, E = 10^{-4}, \tilde{R} = 37$ .

increase for a long time until the field reaches the equilibrium states. The development time of the kinetic energy becomes longer and the kinetic energy at equilibrium state becomes larger as the horizontal scale of the computational domain increases. The increase in kinetic energy over a long period is due to the contribution of the toroidal component. On the other hand, the poloidal energy reaches a steady state soon after the initial development in all cases.

The values of the saturated poloidal kinetic energy are almost independent of  $\lambda$ . This is consistent with previous analyses based on the decomposition of the kinetic energy into the horizontal and the vertical velocity contributions (Favier *et al* 2014, Guervilly *et al* 2014).

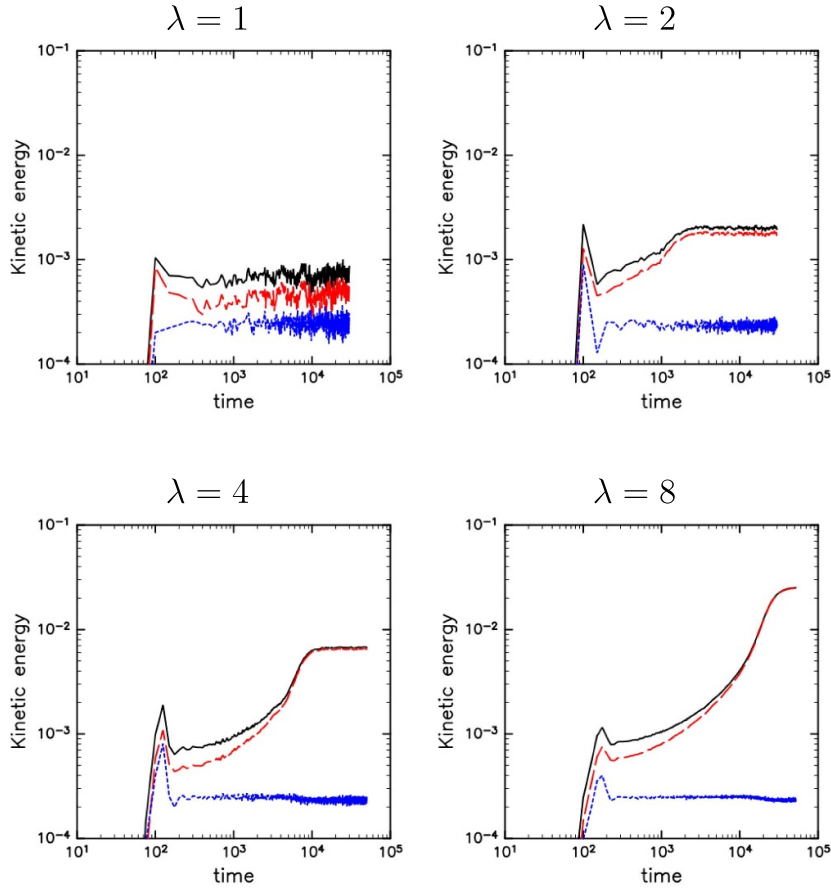


**Figure 3.** Time development of total, toroidal and poloidal kinetic energy,  $\bar{K}$ ,  $\bar{K}^T$  and  $\bar{K}^P$ .  $P = 1, E = 10^{-4}, \tilde{R} = 37$ . Black solid, red broken, and blue dotted lines indicate total, toroidal and poloidal kinetic energy, respectively.

Figure 4 shows the time variation of positive and negative vortex sizes at  $\lambda = 4$ . Here, the vortex size is defined as the number of grid points when adjacent grid points with the same sign of vertical vorticity are connected. This figure reveals asymmetric characteristics depending on the sign of the vorticity. From  $t = 5000$  to  $10000$ , positive vortices develop and become larger, which corresponds to the period where the rapid increase of kinetic energy is observed in the case of  $\lambda = 4$  in figure 3. In contrast, the size of the negative vortices does not change from the initial state. Such horizontal scale difference between positive and negative vortices has not received much attention, and no quantitative analysis has been performed.

The amplitudes of the horizontally averaged horizontal velocity components  $U_x(z, t)$  and  $U_y(z, t)$  excited in the final state are about  $10^{-3}$  instantaneously and about  $10^{-4}$  in time average, which is negligibly small compared to the typical magnitudes of the horizontal velocity components  $u_x$  and  $u_y$ ,  $O(10^{-1})$ .

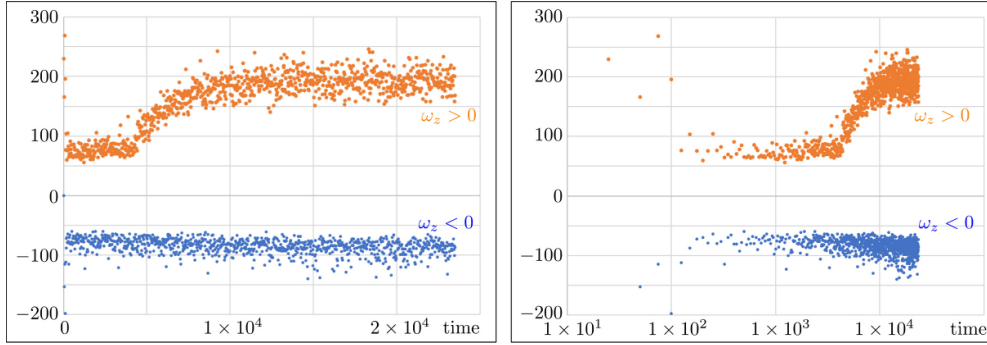


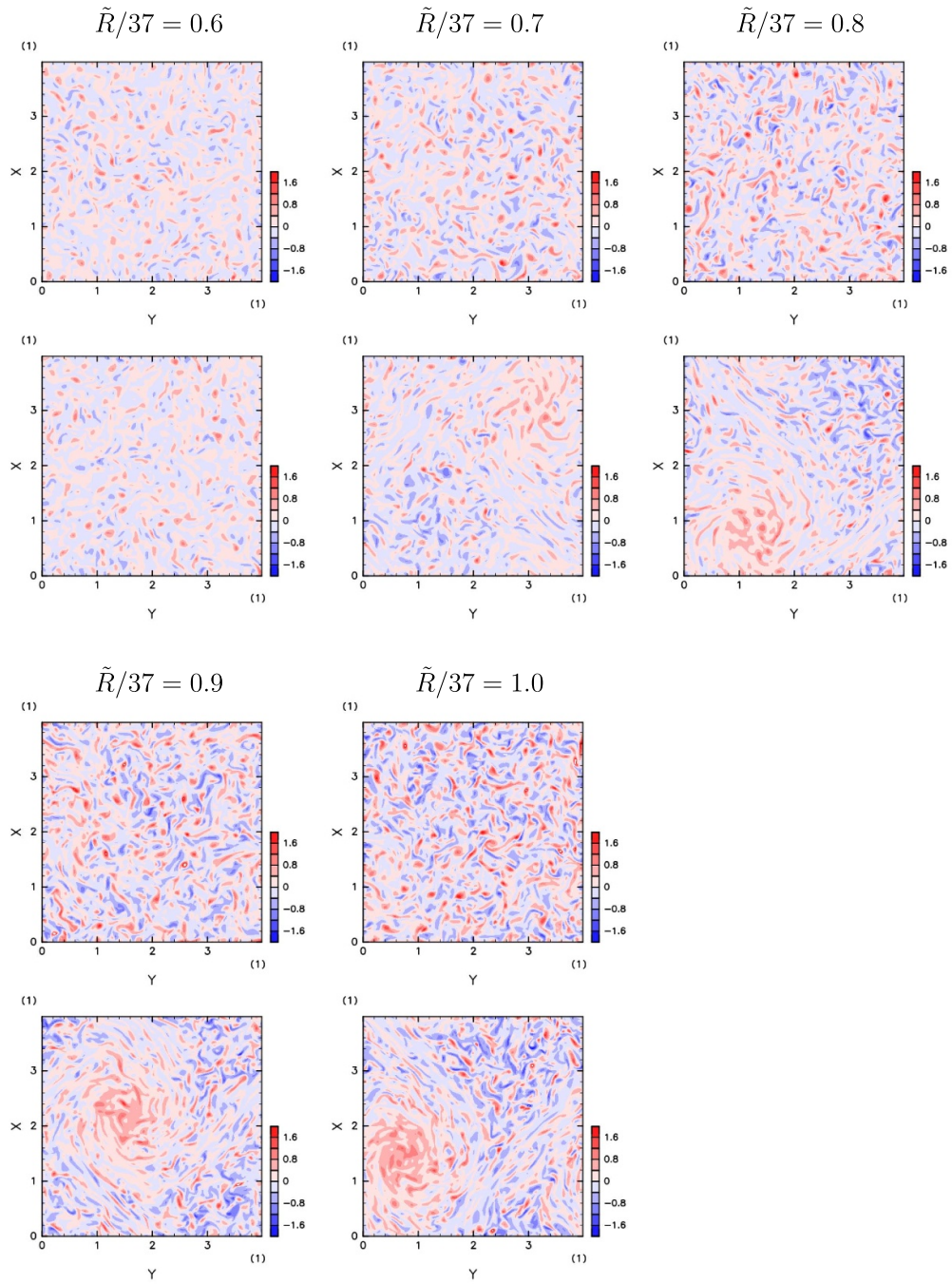
**Figure 4.** Time variation of the size of vortices estimated from the vertical vorticity field at  $z = 0.25$  for the case with  $\lambda = 4$ ,  $P = 1$ ,  $E = 10^{-4}$  and  $\tilde{R} = 37$ . Orange and cyan indicate the number of grid points that are connected with regions  $\omega_z > 0$  and  $\omega_z < 0$  respectively.

### 3.2. Rayleigh number dependence

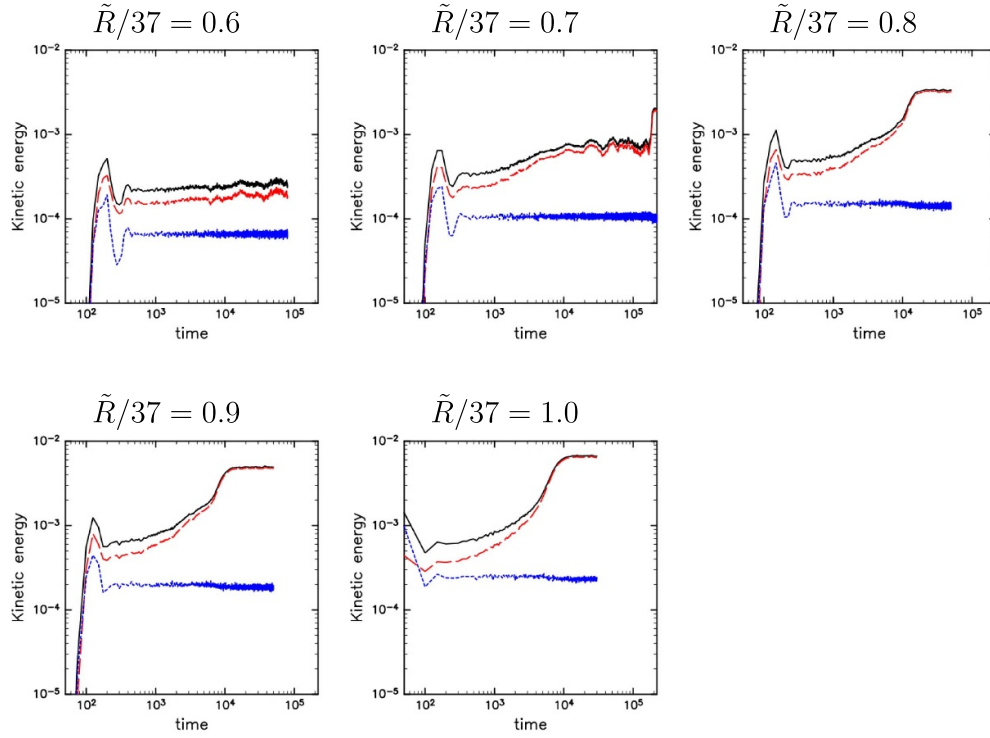
Figure 5 shows the vertical vorticity distributions at the initial and final stages for various values of the Rayleigh number in the case of  $\lambda = 4$ . Initially, as  $\tilde{R}$  increases, stronger small-scale vortices are generated, where their distributions appear to have symmetric property with respect to the sign of the vorticity. In the case of  $\tilde{R}/37 = 0.6$ , the vortex distribution has the same tendency as that of the initial state, and no LSV is observed. In the case of  $\tilde{R}/37 = 0.7$ , we can distinguish between positive and negative LSVs, which occupy approximately 1/4 of the domain, where the distribution is well biased by the sign of the vorticity. With further increases in  $\tilde{R}$ , LSV becomes more distinct, and the coherent vortex structure becomes apparent only in the positive vorticity regions. Such asymmetric development of positive and negative vorticity has been observed in previous studies. Favier *et al* (2014) examined PDFs for the intensity of vertical vorticity, and statistically showed a predominance of the positive vortices, similar to the results of the previous studies (e.g. Julien *et al* 1996). They also examined the vertical distributions of the skewness of the vertical vorticity, and found that the asymmetry is strong at the upper and lower boundaries, suggesting that the asymmetry reflects the characteristics of thermal convection rather than LSVs. Guervilly *et al* (2014) discussed that, as the Rayleigh number increases, the skewness takes  $O(1)$  positive values because of the emergence of LSV. They also showed that the asymmetry does not depend on the initial conditions by performing time integrations starting from the initial conditions where the asymmetry is removed.

Figure 6 shows the time variation of each kinetic energy  $\bar{K}$ ,  $\bar{K}^T$ , and  $\bar{K}^P$  for various Rayleigh numbers in the case of  $\lambda = 4$ . It can be observed that the increase in kinetic energy over a long period of time after the initial linear is suppressed as the Rayleigh number decreases.

The time to reach equilibrium increases with decreasing the Rayleigh number. In particular, for  $\tilde{R}/37 = 0.7$ , the gradual increase in kinetic energy stops at about  $t = 2 \times 10^4$ , but a rapid increase of kinetic energy is observed again at  $t = 2 \times 10^5$ . We confirm that LSV is formed up to  $\tilde{R} = 37 \times 0.7 = 25.9$  by integrating further than  $t = 3 \times 10^5$ . This is about three times larger than the critical Rayleigh number  $\tilde{R}_c = 8.80$ . In all cases, the kinetic energy is dominated by the contribution of the toroidal component while the poloidal energy reaches a steady state soon after the initial development. The values of the poloidal kinetic energy in the statistically



**Figure 5.** Snapshots of vertical vorticity at  $z=0.25$  in the transient (upper panels,  $t=1000$ ) and the final stages (lower panels). Times of the final stage are  $t=80000$ ,  $220000$ ,  $50000$ ,  $50000$ , and  $30000$ , respectively.  $P=1, E=10^{-4}$ .



**Figure 6.** Time development of total, toroidal and poloidal kinetic energy,  $\bar{K}$ ,  $\bar{K}^T$ , and  $\bar{K}^P$  for  $\lambda = 4$ . Black solid, red broken, and blue dotted lines indicate total, toroidal and poloidal kinetic energy, respectively.

equilibrium states increase with increasing the Rayleigh number. The weakening of the dominance of the toroidal kinetic energy with decreasing the Rayleigh number is consistent with the kinetic energy analysis of Guervilly *et al* (2014).

### 3.3. Energy spectral analysis

In this section we investigate quantitatively the formation and maintenance mechanism of LSVs through horizontal spectral analysis of kinetic energy.

Multiplying (9) by  $\psi$  and integrating over the whole domain, we obtain an expression for the time variation of the toroidal kinetic energy.

$$\begin{aligned}
 & -\frac{d}{dt} \int_V dV \frac{1}{2} |\nabla_H \psi|^2 + \int_V dV \psi \mathbf{e}_z \cdot \nabla \times (\mathbf{u} \times \boldsymbol{\omega}) - \int_V dV \psi (\mathbf{e}_z \cdot \nabla) \nabla_H^2 \phi \\
 & = E \int_V dV \psi \nabla_H^2 \nabla^2 \psi.
 \end{aligned} \tag{17}$$

Similarly, multiplying (10) by  $\phi$  and integrating over the whole domain we obtain the expression for the time variation of poloidal kinetic energy.

$$\begin{aligned}
& \int_V dV \frac{1}{2} \frac{\partial}{\partial t} \left[ (\nabla_H^2 \phi)^2 + \left| \nabla_H \frac{\partial \phi}{\partial z} \right|^2 \right] \\
& - \int_V dV \phi \mathbf{e}_z \cdot \nabla \times \nabla \times (\mathbf{u} \times \boldsymbol{\omega}) + \int_V dV \phi (\mathbf{e}_z \cdot \nabla) \nabla_H^2 \psi \\
& = - \int_V dV \phi \frac{RE^2}{P} \nabla_H^2 \theta + E \int_V dV \phi \nabla_H^2 \nabla^2 \nabla^2 \phi, \tag{18}
\end{aligned}$$

where the first term on the left hand side is the time variation of  $\bar{K}^P$ . We decompose the variables in the horizontal direction as follows.

$$\psi = \sum_{l,m} \tilde{\psi}_{l,m}(z,t) e^{2\pi i(lx+my)/\lambda}, \quad \phi = \sum_{l,m} \tilde{\phi}_{l,m}(z,t) e^{2\pi i(lx+my)/\lambda}, \tag{19}$$

which lead to the equations for the time variations of toroidal and poloidal kinetic energy spectra.

$$\frac{dK^T}{dt} = N^T + C^T + V^T, \tag{20}$$

$$\frac{dK^P}{dt} = N^P + C^P + V^P + G^P, \tag{21}$$

where  $K^T$  and  $K^P$  are the toroidal and poloidal kinetic energy spectra.  $N^T$  and  $N^P$  are nonlinear terms,  $C^T$  and  $C^P$  are Coriolis terms, and  $V^T$  and  $V^P$  are viscous terms which contribute to time variations of toroidal and poloidal kinetic energy, respectively.  $G^P$  is the poloidal kinetic energy generation term due to buoyancy. These terms are expressed as follows.

$$K^T(l,m,t) = \frac{1}{2} \int_0^1 dz \frac{4\pi^2}{\lambda^2} (l^2 + m^2) |\tilde{\psi}_{l,m}|^2, \tag{22}$$

$$K^P(l,m,t) = \frac{1}{2} \int_0^1 dz \left[ \frac{16\pi^4}{\lambda^4} (l^2 + m^2)^2 |\tilde{\phi}_{l,m}|^2 + \frac{4\pi^2}{\lambda^2} (l^2 + m^2) \left| \frac{\partial \tilde{\phi}_{l,m}}{\partial z} \right|^2 \right], \tag{23}$$

$$N^T(l,m,t) = \frac{1}{\lambda^2} \int_V dV \tilde{\psi}_{-l,-m} e^{-2\pi i(lx+my)/\lambda} \mathbf{e}_z \cdot \nabla \times (\mathbf{u} \times \boldsymbol{\omega}) \tag{24}$$

$$C^T(l,m,t) = - \frac{1}{\lambda^2} \int_V dV \tilde{\psi}_{-l,-m} e^{-2\pi i(lx+my)/\lambda} (\mathbf{e}_z \cdot \nabla) \nabla_H^2 \phi, \tag{25}$$

$$V^T(l,m,t) = - \frac{1}{\lambda^2} \int_V dV \tilde{\psi}_{-l,-m} e^{-2\pi i(lx+my)/\lambda} E \nabla_H^2 \nabla^2 \psi, \tag{26}$$

$$N^P(l,m,t) = \frac{1}{\lambda^2} \int_V dV \tilde{\phi}_{-l,-m} e^{-2\pi i(lx+my)/\lambda} \mathbf{e}_z \cdot \nabla \times \nabla \times (\mathbf{u} \times \boldsymbol{\omega}), \tag{27}$$

$$C^P(l,m,t) = - \frac{1}{\lambda^2} \int_V dV \tilde{\phi}_{-l,-m} e^{-2\pi i(lx+my)/\lambda} (\mathbf{e}_z \cdot \nabla) \nabla_H^2 \psi, \tag{28}$$

$$V^P(l,m,t) = \frac{1}{\lambda^2} \int_V dV \tilde{\phi}_{-l,-m} e^{-2\pi i(lx+my)/\lambda} E \nabla_H^2 \nabla^2 \nabla^2 \phi, \tag{29}$$

$$G^P(l,m,t) = - \frac{1}{\lambda^2} \int_V dV \tilde{\phi}_{-l,-m} e^{-2\pi i(lx+my)/\lambda} \frac{RE^2}{P} \nabla_H^2 \theta. \tag{30}$$

The total kinetic energy spectrum excluding mean flow contribution  $K(l,m,t)$  becomes,

$$K(l,m,t) = K^T(l,m,t) + K^P(l,m,t). \tag{31}$$

Figure 7 shows  $K$ ,  $K^T$  and  $K^P$  for various values of  $\lambda$  as a function of the total horizontal wavenumber  $k = 2\pi\sqrt{l^2 + m^2}/\lambda$ . In the case of  $\lambda = 1$ , there is no significant change in the spectral distributions between the initial and final states. The energy of the lowest wavenumber

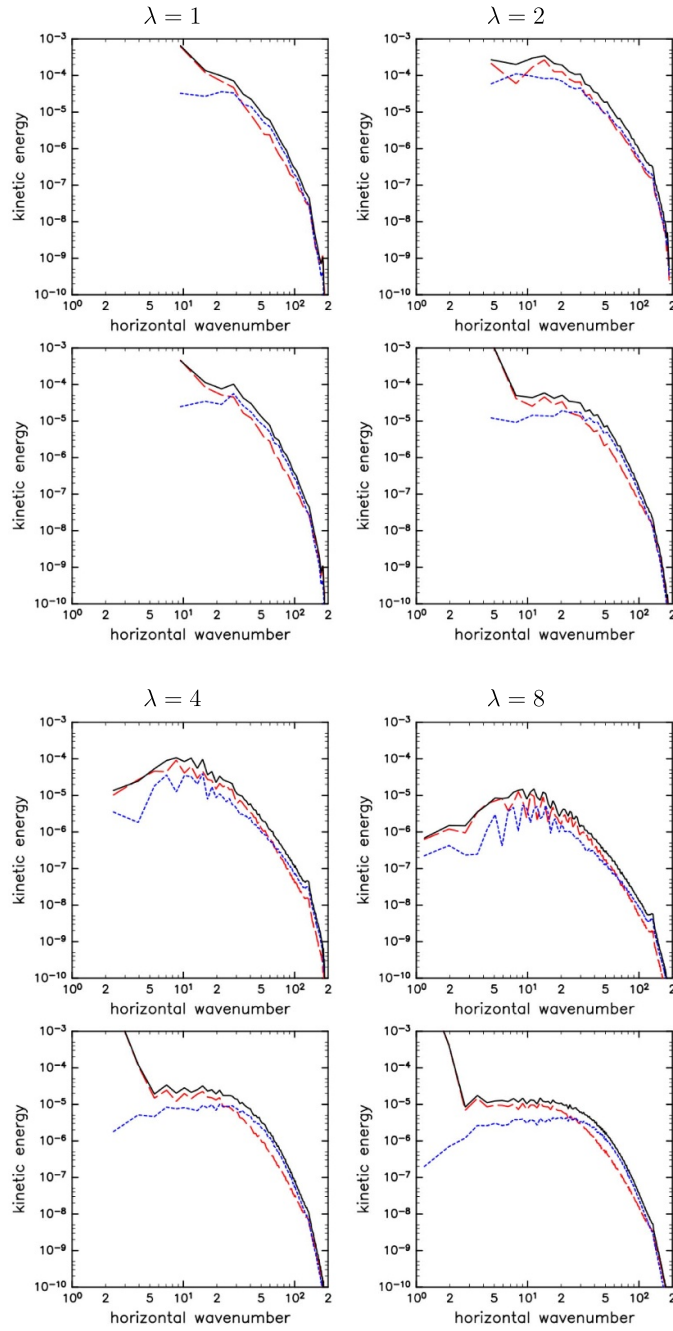


**Figure 7.** The kinetic energy spectrum for various values of  $\lambda$  in the case of  $\tilde{R} = 37$ . The upper and lower panels show the spectrum at  $t = 100$  and in the final state. The horizontal axis is the total horizontal wavenumber  $k = 2\pi\sqrt{l^2 + m^2}/\lambda$ . The solid black, dashed red, and dotted blue lines are  $K(k, t)$ ,  $K^T(k, t)$ , and  $K^P(k, t)$ , respectively.

component is already maximum in the initial state. The toroidal component dominates for low wavenumbers  $k < 30$ , while the poloidal component dominates for high wavenumbers  $k > 30$ . For  $\lambda = 2$ , there is an initial peak at around  $k = 10$ , while the energy is concentrated at the lowest wavenumber due to the toroidal component in the final state. As the horizontal region expands with increasing  $\lambda$  to 4 and 8, the peak at the initial wavenumber of about 10 becomes more pronounced. In the final state, the energy at the lowest wavenumber is prominent, and at lower wavenumbers up to about  $k < 20$ , the toroidal component dominates with similar amplitudes (flat spectral curves) whereas at  $k > 20$ , the poloidal component dominates with decreasing amplitude with a power law of  $-3$  or steeper.

Figure 8 shows the balance of the kinetic energy spectrum for various values of  $\lambda$ . From the lower panels of figure 8, we can see that the buoyancy force (green dotted line) generates poloidal energy for small-scale convective motion centered at  $k = 20$ . It is then reduced by viscous dissipation (red dashed line), and the remainder is converted into small-scale toroidal energy by the Coriolis term (solid black line). Note that this reduction of the poloidal energy by the Coriolis term corresponds to the increase in toroidal energy due to the Coriolis term in the upper panels of figure 8.

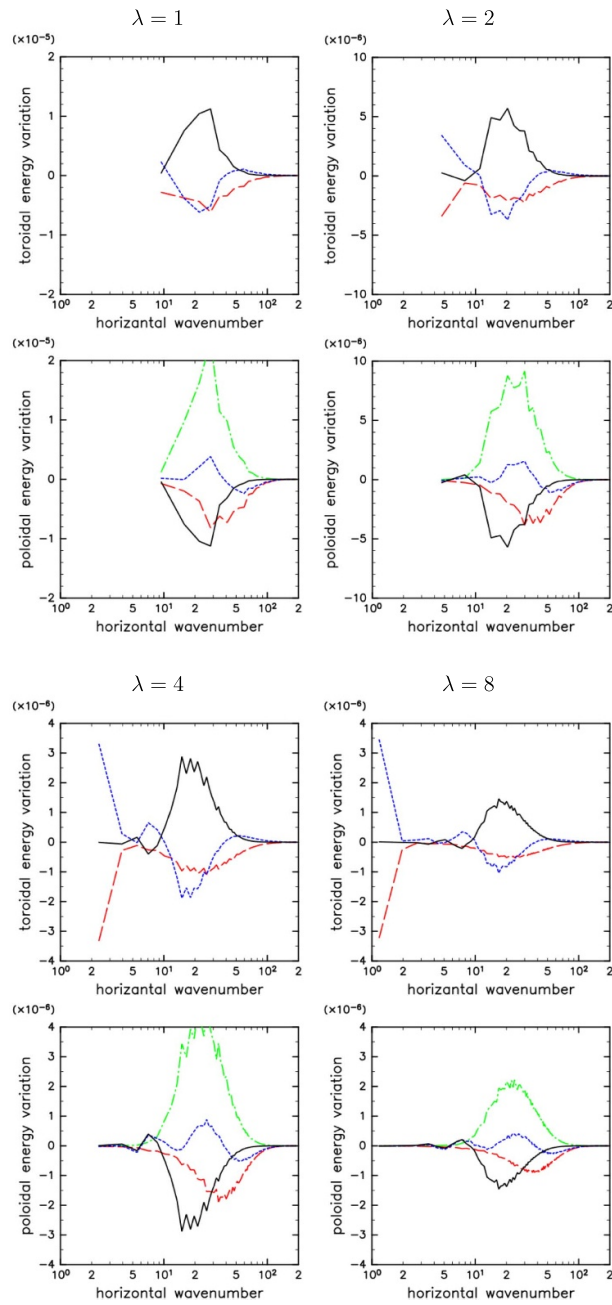
Figure 9 shows the classification of the time variation of the toroidal energy spectrum by the nonlinear term  $N^T(k, t)$  for various  $\lambda$  at  $\tilde{R}/37 = 1.0$ . The velocity and vorticity fields are decomposed into toroidal and poloidal components and their nonlinear effects are shown. From the classification of the non-linear term in  $\lambda = 4$  and 8, we can find that the nonlinear term of the toroidal velocity and toroidal vorticity field  $\mathbf{u}^T \times \boldsymbol{\omega}^T$  contributes to the enhancement of the largest toroidal component. On the other hand, figure 10 shows the classification of the nonlinear effect of the velocity and vorticity fields by their horizontal scales. Here the large and small horizontal scales are separated at a horizontal wavenumber of 10, because the excited small-scale convective motion is observed to have a component with a horizontal wavenumber greater than 10. It can be seen that the non-linear effect of the the small scale velocity and small scale vorticity fields contribute most to the excitation of the largest toroidal motion. This is consistent with the suggestion from the horizontal spectral analysis in the previous studies (Favier *et al* 2014, Guervilly *et al* 2014, Rubio *et al* 2014, Julien *et al* 2018).

### 3.4. Correlation analysis

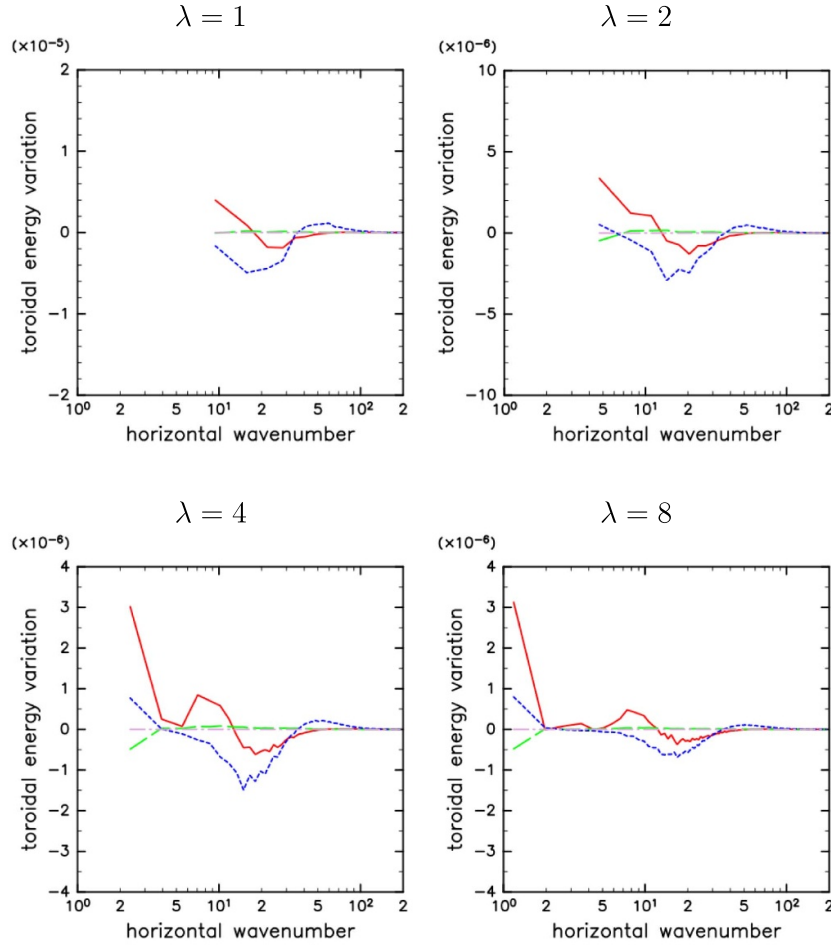
In this subsection, we investigate the characteristics of thermal convection and large-scale vortices by performing statistical correlation analysis between the large and small horizontal scale components of the variables at different heights. As in the previous section, the large and small horizontal scales are separated at the horizontal wavenumber of 10.

Figure 11 shows the horizontally large- and small-scale fields of vertical vorticity, vertical velocity, and temperature disturbances in the case of  $\lambda = 4$  and  $\tilde{R}/37 = 1.0$ . It is found that the amplitudes of small-scale vertical vorticity, vertical velocity, and temperature disturbance are weakened in the region of positive LSV, while there is no correlation between large- and small-scale fields except in the region of LSV. The asymmetry in the large-scale vertical vorticity with respect to its sign is observed also, which is consistent with the previous studies performed so far (e.g. Favier *et al* 2014, Guervilly *et al* 2014). The positive vorticity region has a strongly coherent vortex structure, while the distribution of the negative vorticity region is dispersed. This asymmetry may be related to the subcritical behavior of the LSV emergence found by Favier *et al* (2019).

Figure 12 shows the correlations  $\langle \omega(z = 0.25), \omega(z = 0.75) \rangle$  and  $\langle u_z(z = 0.25), u_z(z = 0.75) \rangle$  of large-scale components (upper panels), and small-scale components (lower panels).



**Figure 8.** The budget analysis of kinetic energy spectrum for various values of  $\lambda$  at  $\bar{R}/37 = 1.0$ . Time averaged at statistical equilibrium near the final state. The horizontal axis is the total horizontal wavenumber  $k = 2\pi\sqrt{l^2 + m^2}/\lambda$ . The solid black, dashed red, dotted blue, and dotted green lines are the Coriolis term  $C^*(k)$ , dissipative term  $V^*(k)$ , non-linear term  $N^*(k)$ , and the generating term  $G^P(k)$ , where  $*$  represents subscripts  $T$  or  $P$  to indicate the the toroidal or poloidal terms at the same time. The upper and lower panels show the toroidal and poloidal energy balance, respectively.



**Figure 9.** Contribution of the nonlinear term to the time variation of toroidal energy  $N^T(k, t)$  is divided according to the combination of toroidal and poloidal fields for various values of  $\lambda$  at  $\bar{R}/37 = 1.0$ . Time averaged values at statistical equilibrium near the final state are shown. The contributions from  $\mathbf{u}^T \times \boldsymbol{\omega}^T$ ,  $\mathbf{u}^P \times \boldsymbol{\omega}^P$ ,  $\mathbf{u}^P \times \boldsymbol{\omega}^T$ , and  $\mathbf{u}^T \times \boldsymbol{\omega}^P$  are drawn with a red solid, green broken, blue dotted, and magenta broken-dotted lines, respectively, where the subscripts  $(\ )^T$  and  $(\ )^P$  indicate the toroidal and poloidal components.

Here,  $\langle f, g \rangle$  denotes the correlation coefficient between two horizontal distributions  $f(x, y)$  and  $g(x, y)$  defined by

$$\langle f, g \rangle = \frac{(f, g)}{\sqrt{(f, f)(g, g)}}, \quad (f, g) = \int_0^\lambda \int_0^\lambda dx dy f(x, y) g(x, y). \quad (32)$$

At the large scale, the correlations of vertical vorticity and vertical velocity are positive between  $z=0.25$  and  $z=0.75$ . In particular, the correlation of vertical vorticity is stronger than that of the vertical velocity at the time of LSV formation, suggesting that a barotropic structure dominates in the LSV. On the other hand, at the small-scale, the vertical vorticity is negatively correlated while the vertical velocity is positively correlated, indicating that their

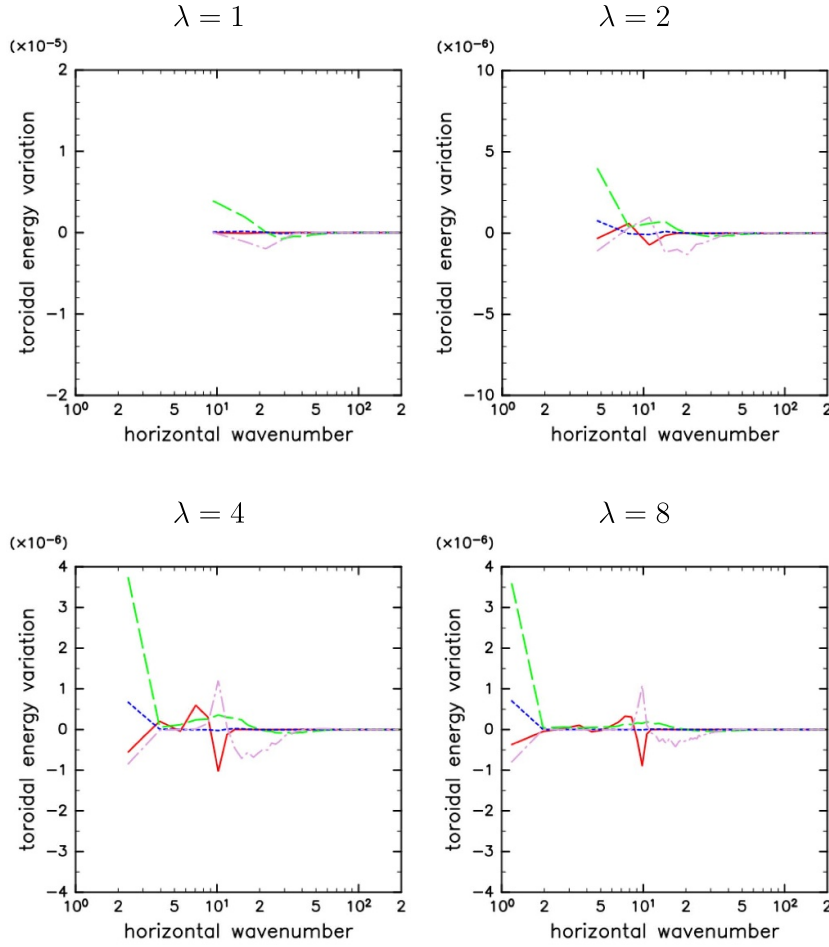


**Figure 10.** Contribution of the nonlinear term to the time variation of toroidal energy  $N^T(k, t)$  is divided according to the combination of large- and small-scale fields for various values of  $\lambda$  at  $\tilde{R}/37 = 1.0$ . Time averaged values at statistical equilibrium near the final state are shown. The contributions from  $\mathbf{u}^L \times \boldsymbol{\omega}^L$ ,  $\mathbf{u}^S \times \boldsymbol{\omega}^S$ ,  $\mathbf{u}^S \times \boldsymbol{\omega}^L$ , and  $\mathbf{u}^L \times \boldsymbol{\omega}^S$  are drawn with a red solid, green broken, blue dotted, and magenta broken-dotted lines, respectively, where the subscripts  $(\ )^L$  and  $(\ )^S$  indicate the horizontally large- and small-scale fields.

structure is dominated by baroclinic vortices. This is consistent with the structure of thermal convection in the rotating system (e.g. Sakai 1997).

Figure 13 shows the time variation of the correlation between the positive and negative large-scale vertical vorticity and the small-scale vertical velocity squared mean at  $z = 0.25$ . The correlations with the positive and negative vorticity are similar in the initial period, while the correlation with positive vorticity decreases over time. This reflects the suppression of small-scale convective motion in the positive LSV.

Figures 14 and 15 show the correlation of the temperature field with the vertical velocity and with the vertical vorticity at several heights. The temperature fields are strongly correlated with the small-scale vertical velocity and vertical vorticity at the same height,

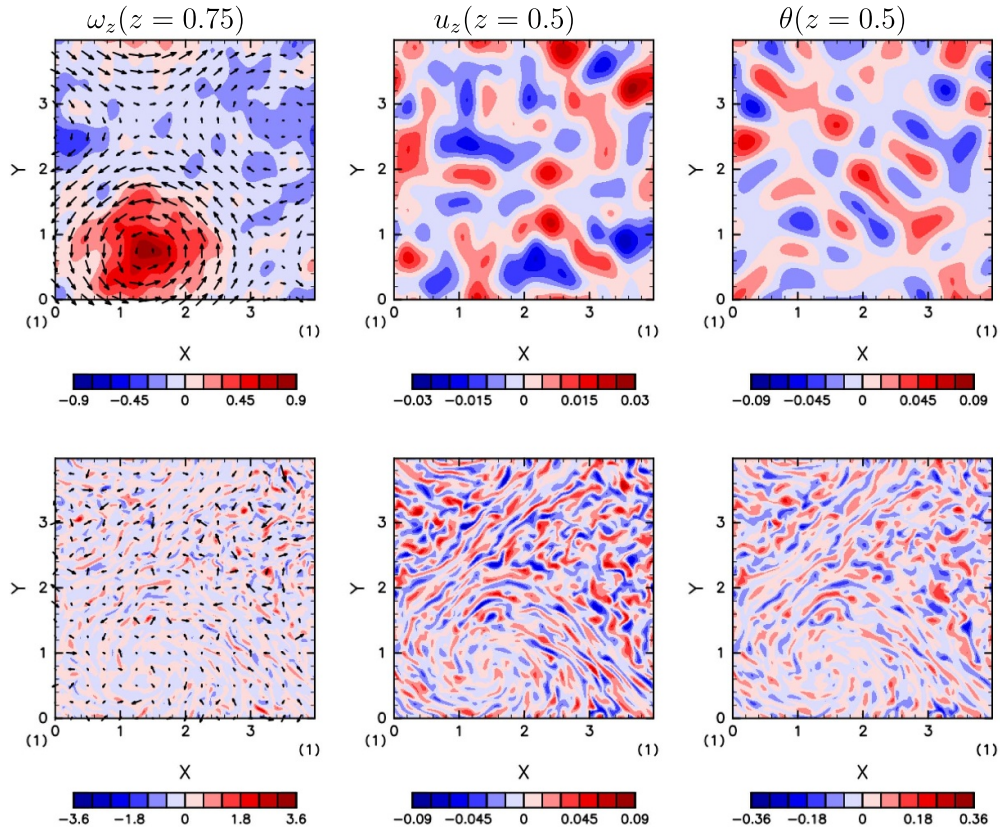


**Figure 11.** Horizontal distributions of various physical quantities separated by large and small horizontal scales in the case of  $\lambda = 4$  and  $\bar{R}/37 = 1.0$ . The upper and lower panels are for large- and small-scale fields, respectively. From left to right, vertical vorticity  $\omega_z$  at  $z = 0.75$ , vertical velocity  $u_z$  at  $z = 0.5$ , and temperature disturbance  $\theta$  at  $z = 0.5$ .

while their correlations at different heights are small. On the other hand, the correlations between temperature and vertical velocity or vorticity on a large-scale are weak for all the combinations.

From the above correlation analysis, it can be concluded that the small-scale field is characterized by a positive correlation between vertical velocity and temperature and a baroclinic vertical vorticity structure, which is consistent with the typical structure of small-scale convection in the rotating system. On the other hand, the large-scale field is characterized by a lack of correlation between vertical velocity and temperature and a barotropic vertical vorticity structure, meaning a two-dimensional vortex structure that has little to do with thermal convection (bottom panel of figure 16).

#### 4. Theoretical diagnoses

In this section, we make theoretical diagnoses for characteristics of small-scale convection and LSVs revealed in section 3.

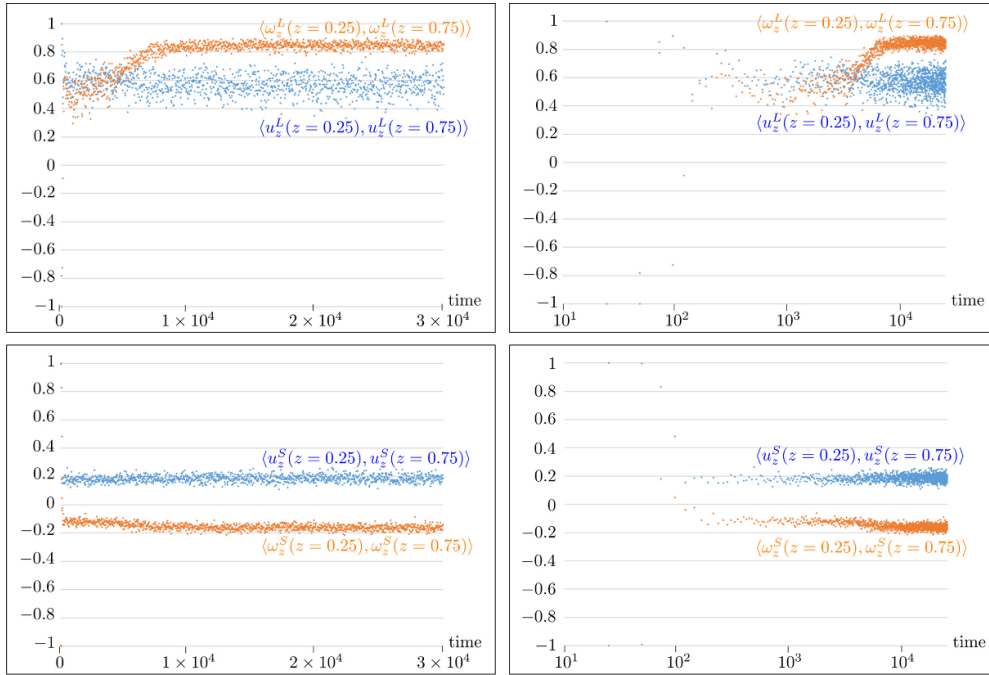


**Figure 12.** Time variation of the vertical correlation of large- and small-scale vertical vorticity and vertical velocity fields,  $\langle \omega_z(z=0.25), \omega_z(z=0.75) \rangle$  and  $\langle u_z(z=0.25), u_z(z=0.75) \rangle$ , for  $\lambda=4$  and  $\tilde{R}/37=1.0$ . Correlations for large- and small-scale components are shown on the upper and lower panels, respectively. Orange and cyan indicate  $\langle \omega_z(z=0.25), \omega_z(z=0.75) \rangle$ , and  $\langle u_z(z=0.25), u_z(z=0.75) \rangle$ , respectively.

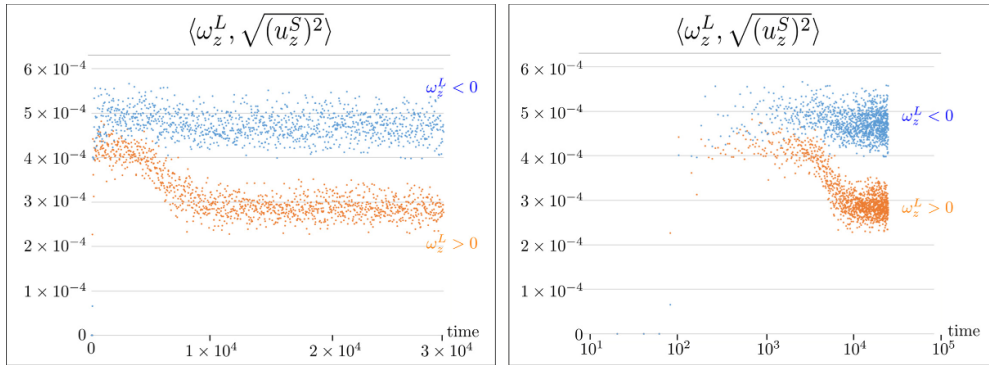


**Figure 13.** Correlation between the large-scale components of the positive and negative vertical vorticity and the small-scale vertical velocity strength  $\langle \omega_z^L(z=0.25), \sqrt{(u_z^S)^2}(z=0.25) \rangle$  for  $\lambda=4$  and  $\tilde{R}/37=1.0$ . Orange and cyan colors indicate the correlation with positive and negative vortices, respectively.

#### 4.1. Linear stability analysis

As seen in figure 11, there emerges active small-scale thermal convection in the large-scale negative vortex region whereas small-scale thermal convection is suppressed in the large-scale

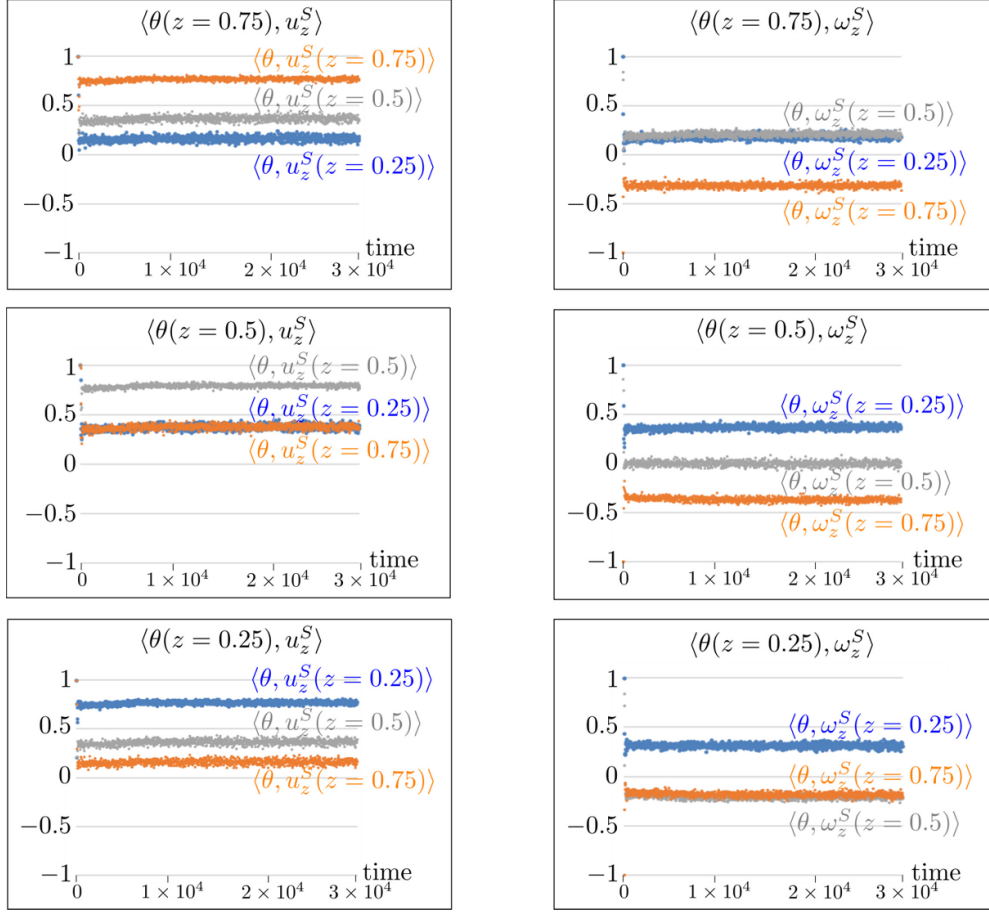


**Figure 14.** Correlations of the temperature field  $\theta$  with small-scale vertical velocity  $u_z$  and vertical vorticity  $\omega_z$  at each height for  $\lambda=4$  and  $\tilde{R}/37 = 1.0$ . From top to bottom, correlations for temperature fields at  $z = 0.75$ ,  $0.5$ , and  $0.25$  are shown. Cyan for  $z = 0.75$ , grey for  $z = 0.5$ , and orange for  $z = 0.25$ .

positive vortex region. This feature is consistent with inhibition of heat transfer in LSV region, possibly because the increase of the effective rotation in the positive vortex region leads suppression of small scale convection (Guervilly *et al* 2014). We try to quantitatively explain this antisymmetry by a linear stability analysis including a local effect of large-scale vortices. Figure 17 compares the growth rates of the linear stability analysis for the stationary field, including the effect of the local rotation of the LSVs. For  $P = 1$ , the growth rate  $\sigma$  for the most unstable vertical mode is written as,

$$\frac{\sigma}{E} = -(k^2 + \pi^2) + \sqrt{R \frac{k^2}{k^2 + \pi^2} - \tilde{T}a \frac{\pi^2}{k^2 + \pi^2}}, \quad (33)$$

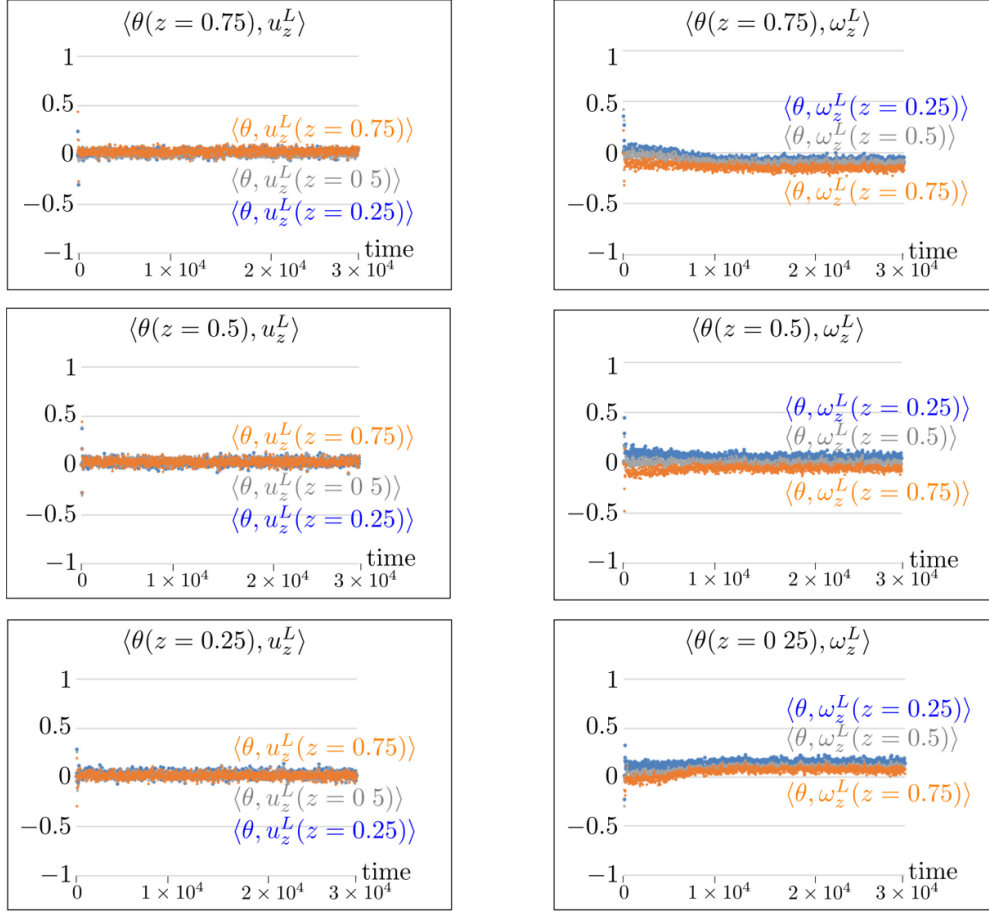


**Figure 15.** Same as figure 14 but for correlations of the temperature field  $\theta$  with large-scale vertical velocity  $u_z$  and vertical vorticity  $\omega_z$ .

where  $k = 2\pi\sqrt{l^2 + m^2}/\lambda$  is the total horizontal wavenumber (appendix A).  $\widetilde{Ta}$  is the Taylor number which takes into account the local effect of large-scale barotropic vertical vorticity on thermal convection by increasing or decreasing the angular velocity of rotation,

$$\widetilde{Ta} = \frac{(1 + Z_b)^2}{E^2}, \quad (34)$$

where  $Z_b$  is a characteristic value of the large-scale vertical vorticity of LSVs in the region of interest. Figure 17 shows the growth rates based on equation (33), where several values of  $Z_b$  are tested in order to assess the effect of LSV on the small-scale convection.

First, we focus on the gross difference between positive and negative LSV regions. Let us apply the average values of positive and negative vorticity of LSVs to  $Z_b$ , which are 1.0 and  $-0.5$ , respectively (figure 2). By comparing the growth rate curves for  $Z_b = 0$  and 1 (solid and dashed lines in the left panel of figure 17), it is expected that small-scale convection with a horizontal wavenumber around 20 is expected to be excited in the absence of the effect of local vorticity, while in the region of LSV with positive vorticity, small-scale convection centered around the horizontal wavenumber 30 will be excited, albeit weakly. On the other hand, the

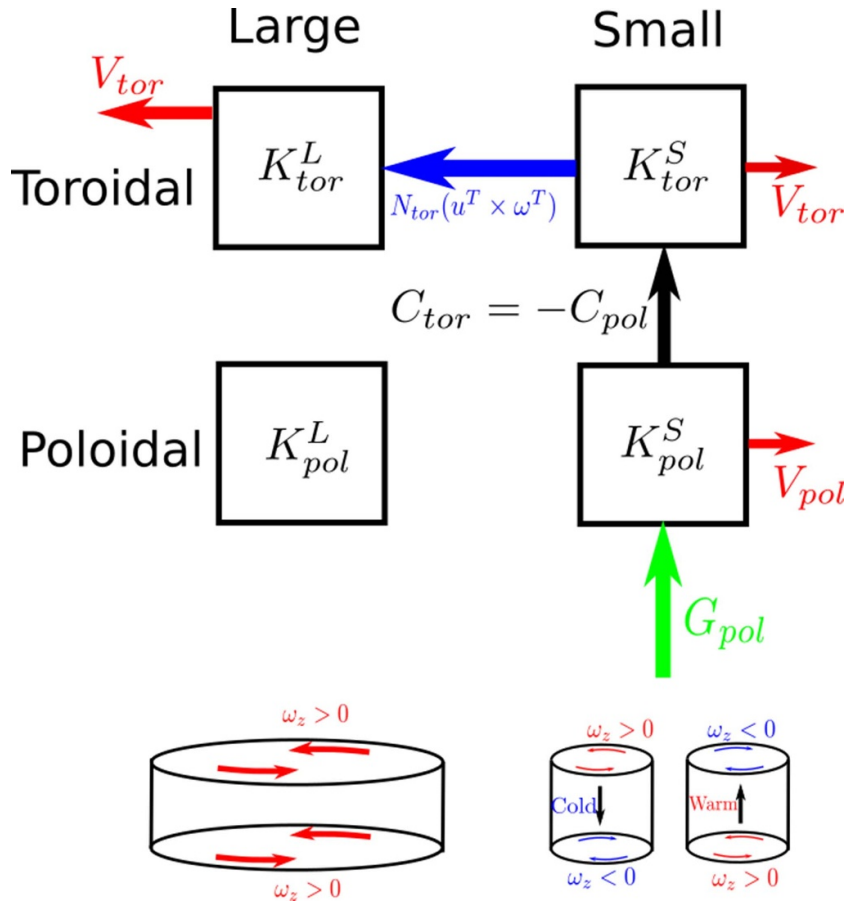


**Figure 16.** The upper panel shows energy flow obtained from energy spectrum balance analysis. The large scale poloidal fields are not important for the generation and maintenance of LSVs, while they may affect the small-scale poloidal fields, which should be investigated by classifying  $N^p$ . The lower panels illustrate the vertical structure of large- and small-fields obtained from correlation analysis. Note that the horizontal shapes of the vortices are not necessarily coin-shaped.

growth rate curve with  $Z_b = -0.5$  (the broken-dashed line in the left panel of figure 17) indicates that convection with a horizontal wavenumber of about 15 is most easily excited in the negative vorticity region, and the horizontal scale of convection in the negative vorticity region is expected to be larger than that in the positive vorticity region.

Next, we turn our attention to the central region of positive LSV. When we take the value of  $Z_b$  as the maximum vorticity of LSV,  $Z_b = 2$  (figure 2), the growth rate is negative for all horizontal wavenumbers (the dotted line in the left panel of figure 17), meaning that thermal convection is expected to be completely suppressed near the center of the positive LSV.

Comparing small-scale convective motions between the LSV with positive vorticity and its outside shown in the small-scale vertical velocity distribution in figure 11, we can find that the difference in the amplitudes and horizontal scales of convection is consistent with the expectation from the linear stability above.

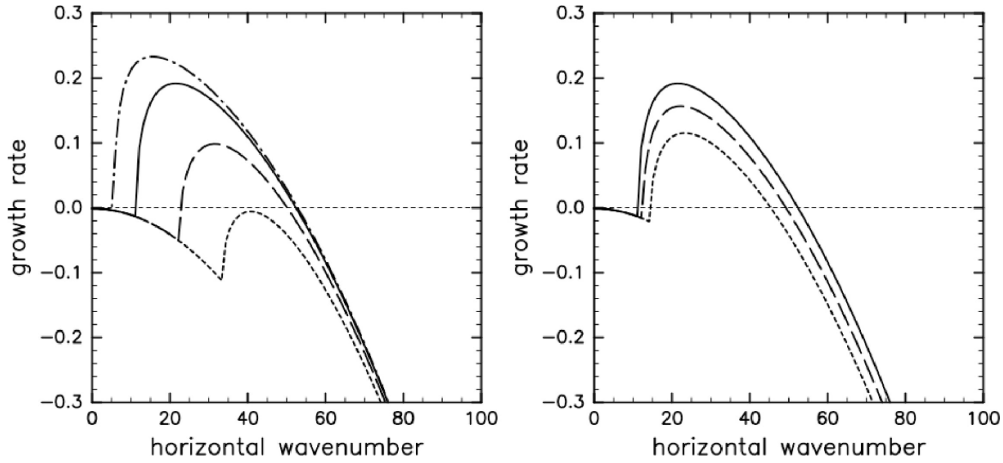


**Figure 17.** The growth rates of the linear stability analysis for stationary fields based on equation (33). The left panel shows the growth rates for  $P = 1$ ,  $\bar{R} = 37$  and  $\lambda = 4$ , including the effect of vorticity of LSV on the rotating convection. The solid line is for global rotation ( $Z_b = 0$ ) only, while the dashed line includes the effect of the average positive vertical vorticity of LSV ( $Z_b = 1$ ), the dotted line includes the effect of the maximum value of the positive vertical vorticity of LSV ( $Z_b = 2.0$ ), and the dash-dotted line includes the effect of the average negative vertical vorticity ( $Z_b = -0.5$ ). The right panel shows the Rayleigh number dependence of the growth rate for  $P = 1$  and  $\lambda = 4$ . The solid, dashed and dotted lines are for  $\bar{R}/37 = 1.0, 0.8$ , and  $0.6$ , respectively.

While the linear stability analysis could capture the asymmetric emergence of small-scale convection, it could not explain the preference for coherent structures in the form of positive LSVs. This seems to be due to some non-linear process depending on the sign of vorticity of LSV. Favier *et al* (2019) started the time integration from the initial field with identical positive and negative LSVs, and found that only the positive LSV survived for a long time while the negative LSV decayed.

#### 4.2. Behavior of large scale barotropic toroidal components

In section 3, it is shown that the large-scale barotropic toroidal components are forced by the nonlinear effect of the small-scale motion, and reach the equilibrium by viscous dissipation. We give a simple physical explanation for the scaling properties of the barotropic toroidal component below.

In order to quantitatively verify this mechanism, we consider the following ordinary differential equation based on the time variation of the toroidal potential (9) (appendix B).

$$\left( \frac{d}{dt} + E\alpha^2 \right) \zeta = f_0(\alpha), \quad (35)$$

where  $\zeta$  is the amplitude of the vertical vorticity with maximum wavelength component of the system (wavenumber  $(l, m) = (1, 0), (0, 1)$ ), and  $\alpha$  is the horizontal wavenumber of LSV, using the horizontal domain size  $\lambda$ , which is given by,

$$\alpha^2 = \frac{4\pi^2}{\lambda^2}. \quad (36)$$

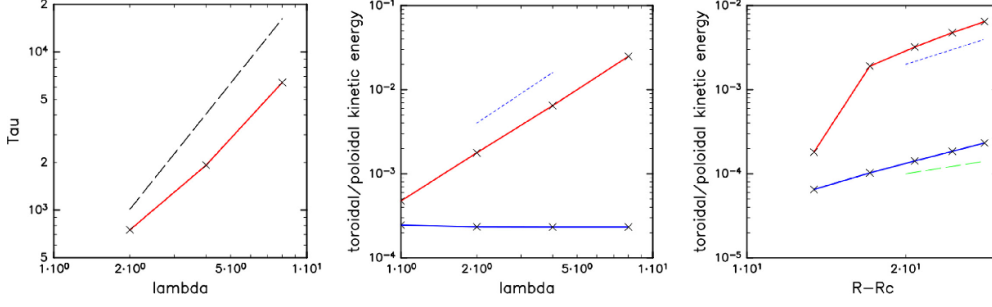


**Figure 18.** Relaxation time versus domain size  $\lambda$  (left), toroidal kinetic energy versus domain  $\lambda$  (center) and  $R - R_c$  (right). The left and center panels are for  $\widetilde{Ra} = 37$  and the right panel is for  $\lambda = 4$ . The black broken line in the left panel shows the viscous time for the horizontally largest barotropic vortices,  $(\lambda/2\pi)^2/E$ . In the center and right, the red solid line represents the toroidal energy, while the blue solid line is the poloidal energy. The blue dotted line indicates the slope for the power of 2 and the green dashed line in the rightmost panel is for the power of 1.

$f_0$  is the contribution of the nonlinear term  $\mathbf{e}_z \cdot \nabla \times (\mathbf{u} \times \boldsymbol{\omega})$  for the components with the wavenumber  $\alpha$  derived from equation (9). With the initial condition  $\zeta(0) = 0$ , we obtain the solution,

$$\zeta = \frac{f_0(\alpha)}{E\alpha^2} \left(1 - e^{-E\alpha^2 t}\right). \quad (37)$$

This approaches  $\zeta(\infty) = f_0/(E\alpha^2)$  as  $t \rightarrow \infty$  with the time scale  $\tau = 1/(E\alpha^2) = \lambda^2/(4\pi^2 E)$ . Then, the kinetic energy of the LSV,  $K_{\text{LSV}}$ , becomes,

$$K_{\text{LSV}} \sim \psi\zeta \sim \alpha^{-2}\zeta^2 = \frac{f_0^2(\alpha)}{E^2\alpha^6}. \quad (38)$$

Figure 18 shows the relaxation time estimated from the time variation of the toroidal energy and the values of the toroidal and poloidal kinetic energy of the statistical equilibrium states in the numerical calculations presented in section 3. From the left panel, we can see that the relaxation time is almost proportional to  $\lambda^2$ , while the middle panel indicates that the toroidal energy is proportional to  $\lambda^2$ . As the kinetic energy of LSV accounts for most of the toroidal energy, this implies that the forcing term  $f_0$  is proportional to  $\alpha^2$ . On the other hand, the poloidal energy does not depend on  $\lambda$ , which again supports the  $\alpha^2$  dependence of  $f_0$  shown in appendix B.2.

We estimated the amplitude of  $f_0(\alpha)$  from the numerical results, and found that the values of  $f_0(\alpha)$  at the final states are roughly in proportion to  $\alpha^2$  although they increase with time (B.2).

Also, from the right panel of figure 18, the poloidal energy is mostly proportional to  $R - R_c$ . This implies that the amplitude of convective motion on small scales is proportional to  $\sqrt{R - R_c}$ . On the other hand, the toroidal energy is proportional to  $(R - R_c)^2$  which is similar to the result of Maffei *et al* (2021) (figure 6c), where the barotropic energy is proportional to  $\widetilde{Ra}$  to the power of about 2. This is consistent with the fact that large scale vortices are directly generated by non-linear effects of vorticity and velocity of the small scale toroidal field discussed in section 3. The small-scale toroidal motion is excited by the small-scale poloidal motion through the Coriolis term, whose amplitude depends on  $\sqrt{R - R_c}$ . The amplitude of the large scale vortex driven by its second order nonlinear effect, and then, is proportional to  $R - R_c$ , resulting in the energy dependence of  $(R - R_c)^2$ .

## 5. Summary

Numerical experiments on three-dimensional Rayleigh–Bénard convection between parallel plates in a rotating system are performed where the horizontal extent of the computational domain is increased compared to those of previous studies. The results confirm the formation of a large-scale vortex with a larger horizontal extent as the horizontal region is extended. The analysis of the kinetic energy by dividing it into the toroidal and poloidal components shows that when the horizontal width of the domain  $\lambda$  becomes larger, the toroidal kinetic energy at statistical equilibrium also becomes larger in proportional to  $\lambda^2$ , and the intensity of LSV increases. On the other hand, the poloidal kinetic energy is smaller than the toroidal kinetic energy and is independent of the horizontal size of the domain. The horizontal spectral analysis of each term in the kinetic energy equation suggests the following mechanism of LSV generation and maintenance. First, the poloidal energy of the small-scale poloidal motion is generated by the buoyancy force, and the Coriolis term converts the energy into small-scale toroidal kinetic energy. When the horizontal extent of the domain is large, the small-scale toroidal motion is converted into the large-scale toroidal component of the kinetic energy by the nonlinear term. This is balanced by the viscous dissipation of the large-scale toroidal motion. This mechanism is consistent with the diagnosis of the dependence of the toroidal kinetic energy on the horizontal size of the domain by a simple model in section 4.2.

In our calculations, the maximally broadened LSV appears even for  $\lambda = 8$ . Our analysis suggests that a maximally broadened LSV appears when the horizontal region is further extended since the viscous dissipation for the largest vortex is so small that the realized kinetic energy is proportional to  $\lambda^2$ , and larger kinetic energy is expected for LSV of larger size. This is similar to what is expected for an inverse cascade in the absence of any additional arrest mechanism.

Our results suggest that one of the key factors in the formation of LSVs is the weak damping effect of viscosity at large scales. This means that, for example, if strong enough damping is effective for larger scales, the emergence of LSVs will be prevented. Let us consider a simple model where the Laplacian dissipation term with respect to vorticity is replaced by a linear dissipation term, such that,

$$\left(\frac{d}{dt} + \gamma\right) \zeta = f_0(\alpha). \quad (39)$$

The solution of this equation becomes,

$$\zeta = \frac{f_0(\alpha)}{\gamma} (1 - e^{-\gamma t}), \quad (40)$$

and the asymptotic solution as  $t \rightarrow \infty$  is  $\zeta(\infty) = f_0/\gamma$ , whose kinetic energy  $K_{\text{LSV}}$  is

$$K_{\text{LSV}} \sim \psi \zeta \sim \alpha^{-2} \zeta^2 = \frac{f_0^2}{\gamma^2 \alpha^2}. \quad (41)$$

If the  $\alpha$  dependence of the forcing term is not significantly different from the Laplacian dissipation case,  $f_0(\alpha) \propto \alpha^2$  and,

$$K_{\text{LSV}} \sim \alpha^2 \propto \lambda^{-2}. \quad (42)$$

Therefore, the kinetic energy decreases as the horizontal scale of the domain increases, implying inhibition of LSV appearance, which indicates the importance of kinetic energy damping mechanism for the generation and maintenance of LSVs.

The analysis of vortex sizes shows that only the positive vortex increases in size, while the size of the negative vortex does not change from the beginning. The vorticity distribution of the large scale field shows that the positive large-scale vortex has a coherent structure

while the negative vorticity field shows no distinct coherent structure. While the linear stability analysis performed in section 4.1 succeeded in qualitatively explaining the asymmetric emergence of small-scale convection on the sign of large-scale vorticity, it is not sufficient for the explanation of the prominence of coherent positive LSVs. We have to conduct finite-amplitude stability analysis of LSVs in order to examine the asymmetric stability depending on the sign of vorticity of the LSV.

In this study, we clarify the mechanism of LSV generation and maintenance. More specifically, we propose a model equation for the mechanism, and predicted the occurrence of LSV for the change of domain. In order to verify these results numerical experiments over a larger horizontal domain should be performed in the future. In addition, only the axisymmetric vortices with the largest scale appear in the horizontally rectangular domain (Guervilly and Hughes 2017). It will be interesting to extend the experimental framework with the horizontal square box presented here to other horizontal shapes of the domain.

## Acknowledgments

We acknowledge the constructive comments from the anonymous reviewers, which helped us improve the manuscript. The present study was supported by the Research Institute for Mathematical Sciences, a Joint Usage/Research Center located in Kyoto University. This work was also supported in part by the Japan Society for the Promotion of Science (KAKENHI Grant Nos. 17H02860, 21H01155 and 23K20878). The numerical calculations were performed on the computer systems of ACCMS, Kyoto University and the Research Institute for Mathematical Sciences, Kyoto University. The library ‘gtool5’ (Ishiwatari *et al* 2012) was used for input and output of numerical data. The products of the Dennou-Ruby project ([www.gfd-dennou.org/arch/ruby/](http://www.gfd-dennou.org/arch/ruby/)) were used for drawing some figures.

## Appendix A. Growth rate of linear stability problem

In the linear stability problem of rotating convection with respect to the quiescent conductive state an analytical expression for the growth rate is obtained for  $P = 1$ . The linear disturbance equations of (9)–(11) becomes as follows.

$$\frac{\partial}{\partial t} \nabla_H^2 \psi - \frac{\partial}{\partial z} \nabla_H^2 \phi = E \nabla_H^2 \nabla^2 \psi, \quad (\text{A.1})$$

$$\frac{\partial}{\partial t} \nabla_H^2 \nabla^2 \phi + \frac{\partial}{\partial z} \nabla_H^2 \psi = -\frac{RE^2}{P} \nabla_H^2 \theta + E \nabla_H^2 \nabla^2 \nabla^2 \phi, \quad (\text{A.2})$$

$$\frac{\partial \theta}{\partial t} + \nabla_H^2 \phi = \frac{E}{P} \nabla^2 \theta. \quad (\text{A.3})$$

The boundary conditions are (12). The variables are expanded by the functional systems satisfying boundary conditions, such that,

$$\psi = \sum_{l,m,n} \hat{\psi}_{l,m,n} e^{2\pi i(lx+my)/\lambda} \cos(n\pi z) e^{\sigma t}, \quad (\text{A.4})$$

$$\phi = \sum_{l,m,n} \hat{\phi}_{l,m,n} e^{2\pi i(lx+my)/\lambda} \sin(n\pi z) e^{\sigma t}, \quad (\text{A.5})$$

$$\theta = \sum_{l,m,n} \hat{\theta}_{l,m,n} e^{2\pi i(lx+my)/\lambda} \sin(n\pi z) e^{\sigma t}. \quad (\text{A.6})$$

where  $n$  is the vertical mode number and  $\sigma$  is the complex growth rate. Substituting these expressions into (A.1)–(A.3), and operating  $\int_0^1 dz \cos(n'\pi z)$  and  $\int_0^1 dz \sin(n'\pi z)$ , independent third-order eigenequations are obtained for each  $n$ .

$$\begin{pmatrix} \sigma k^2 + Ek^2 k_n^2 & -n\pi k^2 & 0 \\ n\pi k^2 & -\sigma k^2 k_n^2 - Ek^2 k_n^4 & -\frac{RE^2}{P} k^2 \\ 0 & k^2 & -\sigma - \frac{E}{P} k_n^2 \end{pmatrix} \begin{pmatrix} \hat{\psi} \\ \hat{\phi} \\ \hat{\theta} \end{pmatrix} = 0, \quad (\text{A.7})$$

where  $k = 2\pi\sqrt{l^2 + m^2}/\lambda$  is the total horizontal wavenumber, and  $k_n^2 = k^2 + n^2\pi^2$  is the square of the total wavenumber. For non-trivial solutions to exist, we have

$$\left(\sigma + Ek_n^2\right)^2 \left(\sigma + \frac{E}{P} k_n^2\right) + \left(\sigma + Ek_n^2\right) \frac{n^2\pi^2}{k_n^2} - \left(\sigma + \frac{E}{P} k_n^2\right) \frac{RE}{P} \frac{k^2}{k_n^2} = 0. \quad (\text{A.8})$$

In particular, when  $P = 1$ ,

$$\frac{\sigma}{E} = -k_n^2, \quad -k_n^2 \pm \sqrt{R \frac{k^2}{k_n^2} - \frac{1}{E^2} \frac{n^2\pi^2}{k_n^2}}. \quad (\text{A.9})$$

Rewriting  $n = 1$ ,  $Ta = 1/E^2$  and choosing the solution that  $\sigma > 0$ , we obtain,

$$\frac{\sigma}{E} = -k_1^2 + \sqrt{R \frac{k^2}{k_1^2} - Ta \frac{\pi^2}{k_1^2}}. \quad (\text{A.10})$$

Replacing  $Ta$  by  $\widetilde{Ta}$ , which includes the effect of local vortex rotation, we obtain (33).

## Appendix B. LSV model

### B.1. Derivation of model

The governing equation for LSV model is based on the low wavenumber components of the toroidal equation (9). By applying  $\int_0^1 dz$  to (9) in order to extract the barotropic mode, the contribution of the Coriolis term is eliminated with the boundary condition  $\phi = 0$  at  $z = 0, 1$ , and obtain,

$$\frac{\partial}{\partial t} \nabla_H^2 \bar{\psi} + \overline{\mathbf{e}_z \cdot \nabla \times (\mathbf{u} \times \boldsymbol{\omega})} = E \nabla_H^2 \nabla^2 \bar{\psi}. \quad (\text{B.1})$$

where  $\bar{(\ )}$  indicates vertically averaged quantity such that,

$$\bar{f}(x, y, t) = \int_0^1 f(x, y, z, t) dz. \quad (\text{B.2})$$

Further, as same as (19), the variables are expanded with the double Fourier series, we obtain,

$$\frac{\partial}{\partial t} \tilde{\zeta}_k + E |\mathbf{k}|^2 \tilde{\zeta}_k = N_k. \quad (\text{B.3})$$

Here,  $\mathbf{k} = (k_x, k_y)$  is the horizontal wavenumber vector,  $\mathbf{x} = (x, y)$  is the horizontal position vector, and,

$$N_{\mathbf{k}} = -\frac{1}{4\pi^2\lambda^2} \int_0^\lambda \int_0^\lambda dx dy \overline{e_z \cdot \nabla \times (\mathbf{u} \times \boldsymbol{\omega})} e^{-i\mathbf{k} \cdot \mathbf{x}}. \quad (\text{B.4})$$

By integrating this expression along the circle of the maximum horizontal wavenumber  $\alpha = |\mathbf{k}|$  in the wavenumber space, we obtain the LSV model equation (B.5).

$$\left( \frac{d}{dt} + E\alpha^2 \right) \zeta = f_0, \quad (\text{B.5})$$

where,

$$\zeta = \oint \alpha d\theta \zeta_{\mathbf{k}, |\mathbf{k}|=\alpha}, \quad f_0(\alpha) = \oint \alpha d\theta N_{\mathbf{k}, |\mathbf{k}|=\alpha}. \quad (\text{B.6})$$

Here,  $(\alpha, \theta)$  is the polar coordinates of the wavenumber space so that  $k_x = \alpha \cos \theta$  and  $k_y = \alpha \sin \theta$ .

## B.2. Scaling of LSV

As discussed in section 4.2, the forcing term  $f_0(\alpha)$  must be proportional to  $\alpha^2$  in order to explain  $\lambda$  dependence of the toroidal and poloidal energies of the LSV model. This is consistent with the fact that the poloidal energy is independent of  $\lambda$ , i.e. independent of the amplitude of the small-scale thermal convection. Based on this fact, we evaluate the dependence of the nonlinear effect of the two variables on  $\lambda$  associated with small-scale thermal convection. We pay attention to the integrand of the representation of  $N_{\mathbf{k}}$  in (B.4). This term is expressed as a sum of the products of two variables whose spectral peaks are located at higher wavenumbers compared to the horizontal wavenumbers of the LSV. Let their horizontal spectral distributions be  $\tilde{f}(\mathbf{k})$  and  $\tilde{g}(\mathbf{k})$  such that,

$$f(\mathbf{x}) = \sum_{\mathbf{k}_1} \tilde{f}(\mathbf{k}_1) e^{i\mathbf{k}_1 \cdot \mathbf{x}}, \quad g(\mathbf{x}) = \sum_{\mathbf{k}_2} \tilde{g}(\mathbf{k}_2) e^{i\mathbf{k}_2 \cdot \mathbf{x}}. \quad (\text{B.7})$$

Then, the contribution of each product  $T_{\mathbf{k}} = \tilde{f}\tilde{g}(\mathbf{k})$  becomes,

$$T_{\mathbf{k}} = \frac{1}{4\pi^2\lambda^2} \int_0^\lambda \int_0^\lambda dx dy e^{-i\mathbf{k} \cdot \mathbf{x}} \sum_{\mathbf{k}_1} \tilde{f}(\mathbf{k}_1) e^{i\mathbf{k}_1 \cdot \mathbf{x}} \sum_{\mathbf{k}_2} \tilde{g}(\mathbf{k}_2) e^{i\mathbf{k}_2 \cdot \mathbf{x}}. \quad (\text{B.8})$$

Since this integral is only from the  $\mathbf{k}_1 + \mathbf{k}_2 - \mathbf{k} = 0$  components, we have,

$$T_{\mathbf{k}} = \frac{1}{4\pi^2\lambda^2} \int_0^\lambda \int_0^\lambda dx dy \sum_{\mathbf{k}_1} \tilde{f}(\mathbf{k}_1) \tilde{g}(\mathbf{k} - \mathbf{k}_1). \quad (\text{B.9})$$

Since  $|\mathbf{k}| \ll |\mathbf{k}_1|$ , the wavenumbers are approximated as  $\mathbf{k} - \mathbf{k}_1 \sim -\mathbf{k}_1$ , and then,

$$T_{\mathbf{k}} \sim \frac{1}{4\pi^2\lambda^2} \int_0^\lambda \int_0^\lambda dx dy \sum_{\mathbf{k}_1} \tilde{f}(\mathbf{k}_1) \tilde{g}(-\mathbf{k}_1) = \frac{1}{4\pi^2} \sum_{\mathbf{k}_1} \tilde{f}(\mathbf{k}_1) \tilde{g}(-\mathbf{k}_1). \quad (\text{B.10})$$

Because the small-scale thermal convection in the numerical simulations is assumed to have a locally structure and amplitude are considered to be locally determined, the mean kinetic energy  $E^P$  does not change with  $\lambda$ , which can be confirmed from the middle panel of figure 18. Then, since  $E^P$  is expressed by the form of  $\sum_{\mathbf{k}} |\tilde{f}(\mathbf{k})|^2$  and the number of sums for  $\mathbf{k}$  is proportional to  $\lambda^2$ ,  $|\tilde{f}(\mathbf{k})|^2$  must be proportional to  $\lambda^{-2}$  for  $E^P$  to be independent of  $\lambda$ . Therefore,  $|\tilde{f}(\mathbf{k})|$

is proportional to  $\lambda^{-1}$ . Considering that all small-scale convection-related spectral coefficients are proportional to  $\lambda^{-1}$ , the  $\lambda$  dependence of the nonlinear term  $T_k$  becomes,

$$T_k \sim \sum_k \tilde{f}(\mathbf{k}) \tilde{g}(-\mathbf{k}) \propto \lambda^2 (\lambda^{-1})^2 \sim \text{const}, \quad (\text{B.11})$$

which does not depend on the size  $\lambda$  or  $\alpha$ . Thus, the small scale of  $\mathbf{u} \times \boldsymbol{\omega}$  is considered to be independent of  $\alpha$ . Evaluating the operator  $\mathbf{e}_z \cdot \nabla \times$  in (B.4),  $N_{k,|k|=\alpha} \propto \alpha$ , and then, from (B.6),  $f_0(\alpha) \propto \alpha^2$ .

We estimated the amplitude of  $f_0(\alpha)$  by evaluating the contribution of the nonlinear term to the smallest wavenumber components of toroidal kinetic energy,  $\hat{N}^T(\alpha, t) = N^T(0, \pm 1, t) + N^T(\pm 1, 0, t)$ , for the cases with  $\lambda = 1, 2, 4$  and  $8$ , where  $N^T(l, m, t)$  is defined by (24). Although  $\hat{N}^T(\alpha, t)$  increases with time, the values at the final state are roughly independent of  $\alpha$ , meaning that  $f_0(\alpha)$  is in proportion to  $\alpha^2$ .  $N_{k,|k|=\alpha}$  in (B.6) can be evaluated by the relation,  $\hat{N}^T(\alpha, t) \sim \tilde{\psi}_\alpha N_{k,|k|=\alpha}$ . From  $\lambda$  dependence of toroidal kinetic energy,  $\tilde{\psi}_\alpha^2 \sim \lambda^2 \sim 1/\alpha^2$ , then  $N_{k,|k|=\alpha} \sim \alpha$  leading to  $f_0(\alpha) \sim \alpha^2$  from (B.6).

## ORCID iD

Shin-ichi Takehiro  <https://orcid.org/0000-0002-0857-3992>

## References

- Chan K L 2007 Rotating convection in f-boxes: faster rotation *Astron. Nachr.* **328** 1059–61
- Chan K L and Mayr H G 2013 Numerical simulation of convectively generated vortices: application to the Jovian planets *Earth Planet. Sci. Lett.* **371** 212–9
- Chandrasekhar S 1961 *Hydrodynamic and Hydromagnetic Stability* (Oxford University Press) p 652
- de Wit X M, Guzmán A J A, Clercx H J and Kunnen R P 2022 Discontinuous transitions towards vortex condensates in buoyancy-driven rotating turbulence *J. Fluid Mech.* **936** A43
- Favier B, Guervilly C and Knobloch E 2019 Subcritical turbulent condensate in rapidly rotating Rayleigh-Bénard convection *J. Fluid Mech.* **864** R1
- Favier B, Silvers L J and Proctor M R E 2014 Inverse cascade and symmetry breaking in rapidly-rotating Boussinesq convection *Phys. Fluids* **26** 096605
- Guervilly C and Hughes D W 2017 Jets and large-scale vortices in rotating Rayleigh-Bénard convection *Phys. Rev. Fluids* **2** 113503
- Guervilly C, Hughes D W and Jones C A 2014 Large-scale vortices in rapidly rotating Rayleigh-Bénard convection *J. Fluid Mech.* **758** 407–35
- Ishiwatari M et al 2012 Gtool development group, 2012: Gtool5: a Fortran90 library of input/output interfaces for self-descriptive multi-dimensional numerical data *Geosci. Model Dev.* **5** 449–55
- Julien K and Knobloch E 2007 Reduced models for fluid flows with strong constraints *J. Math. Phys.* **48** 065405
- Julien K, Knobloch E and Plumley M 2018 Impact of domain anisotropy on the inverse cascade in geostrophic turbulent convection *J. Fluid Mech.* **837** R4
- Julien K, Knobloch E and Werner J 1998 A new class of equations for rotationally constrained flows *Theor. Comput. Fluid Dyn.* **11** 251–61
- Julien K, Legg S, McWilliams J and Werner J 1996 Rapidly rotating turbulent Rayleigh-Bénard convection *J. Fluid Mech.* **322** 243–73
- Julien K, Rubio A M, Grooms I and Knobloch E 2012 : Statistical and physical balances in low Rossby number Rayleigh-Bénard convection *Geophys. Astrophys. Fluid Dyn.* **106** 392–428
- Käpylä P J, Mantere M J and Hackman T 2011 Starspots due to large-scale vortices in rotating turbulent convection *Astrophys. J.* **742** 34
- Maffei S, Krüss M, Julien K and Calkins M 2021 On the inverse cascade and flow speed scaling behaviour in rapidly rotating Rayleigh-Bénard convection *J. Fluid Mech.* **913** A18

- Rubio A M, Julien K, Knobloch E and Weiss J B 2014 Upscale energy transfer in three-dimensional rapidly rotating turbulent convection *Phys. Rev. Lett.* **112** 144501
- Sakai S 1997 The horizontal scale of rotating convection in the geostrophic regime *J. Fluid Mech.* **333** 85–95
- Sprague M, Julien K, Knobloch E and Werne J 2006 Numerical simulation of an asymptotically reduced system for rotationally constrained convection *J. Fluid Mech.* **551** 141–74